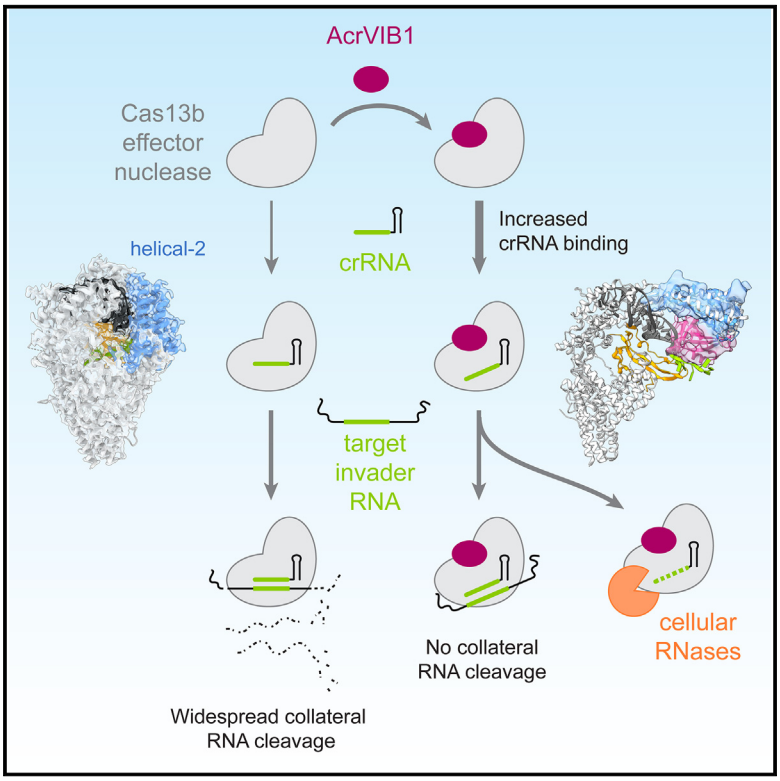
Molecular Cell

Article

# AcrVIB1 inhibits CRISPR-Cas13b immunity by promoting unproductive crRNA binding accessible to RNase attack

## Graphical abstract




## Highlights

- AcrVIB1 binds Cas13b in the absence of a crRNA
- The bound AcrVIB1 promotes crRNA binding to Cas13b
- The crRNA binds Cas13b unproductively and is accessible to RNases
- AcrVIB1 binds the helical-2 domain of Cas13b, preventing it from securing the crRNA

## Authors

Katharina G. Wandera, Stefan Schmelz, Angela Migur, ..., Neva Caliskan, Wulf Blankenfeldt, Chase L. Beisel

## Correspondence

wulf.blankenfeldt@helmholtz-hzi.de (W.B.), chase.beisel@helmholtz-hiri.de (C.L.B.)

## In brief

Wandera et al. report the inhibitory mechanism of AcrVIB1, the only known anti-CRISPR protein against type VI-B CRISPR-Cas systems. They show that the Acr converts the Cas13b effector nuclease into a crRNA sink that enhances crRNA binding but prevents target RNA-mediated activation and leaves the crRNA accessible to host RNases.

Wandera et al., 2025, Molecular Cell *85*, 1–14
March 20, 2025 © 2025 The Author(s). Published by Elsevier Inc.
https://doi.org/10.1016/j.molcel.2025.01.020

CellPress

Please cite this article in press as: Wandera et al., AcrVIB1 inhibits CRISPR-Cas13b immunity by promoting unproductive crRNA binding accessible to RNase attack, Molecular Cell (2025), https://doi.org/10.1016/j.molcel.2025.01.020

Molecular Cell

CellPress
OPEN ACCESS

Article

# AcrVIB1 inhibits CRISPR-Cas13b immunity by promoting unproductive crRNA binding accessible to RNase attack

Katharina G. Wandera,[1] Stefan Schmelz,[2,5] Angela Migur,[1,5] Anuja Kibe,[1,5] Peer Lukat,[2,5] Tatjana Achmedov,[1] Neva Caliskan,[1,6] Wulf Blankenfeldt,[2,3,*] and Chase L. Beisel[1,4,7,*]

[1]Helmholtz Institute for RNA-based Infection Research (HIRI), Helmholtz Centre for Infection Research (HZI), 97080 Würzburg, Germany
[2]Helmholtz Centre for Infection Research (HZI), 38124 Braunschweig, Germany
[3]Institute of Biochemistry, Biotechnology and Bioinformatics, Technische Universität Braunschweig, 38106 Braunschweig, Germany
[4]Medical Faculty, University of Würzburg, 97080 Würzburg, Germany
[5]These authors contributed equally
[6]Present address: Center for Biochemistry, University of Regensburg, 93053 Regensburg, Germany
[7]Lead contact
*Correspondence: wulf.blankenfeldt@helmholtz-hzi.de (W.B.), chase.beisel@helmholtz-hiri.de (C.L.B.)
https://doi.org/10.1016/j.molcel.2025.01.020

## SUMMARY

Anti-CRISPR proteins (Acrs) inhibit CRISPR-Cas immune defenses, with almost all known Acrs acting on the Cas nuclease-CRISPR (cr)RNA ribonucleoprotein (RNP) complex. Here, we show that AcrVIB1 from *Riemerella anatipestifer*, the only known Acr against Cas13b, principally acts upstream of RNP complex formation by promoting unproductive crRNA binding followed by crRNA degradation. AcrVIB1 tightly binds to Cas13b but not to the Cas13b-crRNA complex, resulting in enhanced rather than blocked crRNA binding. However, the more tightly bound crRNA does not undergo processing and fails to activate collateral RNA cleavage even with target RNA. The bound crRNA is also accessible to RNases, leading to crRNA turnover *in vivo* even in the presence of Cas13b. Finally, cryoelectron microscopy (cryo-EM) structures reveal that AcrVIB1 binds a helical domain of Cas13b responsible for securing the crRNA, keeping the domain untethered. These findings reveal an Acr that converts an effector nuclease into a crRNA sink to suppress CRISPR-Cas defense.

## INTRODUCTION

The ancient yet ongoing arms race between bacteria and (bacterio-)phages has led to the evolution of numerous anti-phage defense systems as well as phage-encoded counter-defenses.[1–3] One prevalent pairing comprises CRISPR-Cas systems and anti-CRISPR proteins (Acrs). CRISPR-Cas systems confer adaptive immunity by storing fragments of foreign genetic material expressed as CRISPR RNAs (crRNAs) that guide anti-phage defense by the system's effector nuclease.[4,5] These systems possess a diverse range of molecular mechanisms that confer immune defense, with the current classification scheme dividing CRISPR-Cas systems into 2 classes, 7 types, and over 33 subtypes and variants.[6,7] Acrs are smaller (52–528 amino acids) proteins typically encoded by phages that inhibit different steps of CRISPR-based immunity.[8–10] These protein inhibitors have proven as diverse as CRISPR-Cas systems, with five CRISPR-Cas types and 13 subtypes associated with at least one inhibiting Acr[10] as well as a wide range of inhibitory mechanisms.[11–13]

Within the diversity of inhibitory mechanisms exhibited by Acrs, the vast majority directly act on the ribonucleoprotein (RNP) effector complex formed between a Cas effector nuclease and its crRNA. In one of the most common modes across CRISPR-Cas types, the Acr binds directly to the effector complex to block target recognition or binding. As examples of this mode, AcrIF1 attaches to the hexameric Cas7f backbone within the type I-F effector complex to block hybridization of the crRNA guide to target DNA,[14,15] AcrIIA4 occupies the protospacer-adjacent motif (PAM)-interacting site of the type II effector nuclease Cas9 to prevent DNA interrogation,[16] and AcrVIA1 binds the guide-exposed portion of the type VI-A effector nuclease Cas13a to block hybridization of the crRNA guide to a complementary target RNA.[17] Acrs can also cause the effector complex to non-specifically bind DNA as exemplified by AcrIF9[18] or acetylate the effector complex or the nuclease to block recognition of the PAM flanking the crRNA target as exemplified by AcrVA5.[19] Other Acrs exert their effects on the RNP complex after the complex has bound the target. For instance, AcrIIC4 acts on the Cas9 effector complex after PAM binding but before R-loop formation.[20] Separately, AcrIIA5 acts on the Cas9 effector complex after R-loop formation by blocking the RuvC endonuclease domain.[21] Thus, a wide range of inhibitory


This is an open access article under the CC BY-NC license (http://creativecommons.org/licenses/by-nc/4.0/).

Please cite this article in press as: Wandera et al., AcrVIB1 inhibits CRISPR-Cas13b immunity by promoting unproductive crRNA binding accessible to RNase attack, Molecular Cell (2025), https://doi.org/10.1016/j.molcel.2025.01.020



mechanisms have been elucidated in which an Acr acts on the pre-formed RNP complex.

In contrast, only two mechanisms have emerged that solely act before RNP complex formation. In one mechanism represented by AcrIIC2 and AcrIIA17, the Acr binds to Cas9, occluding crRNA binding.[22,23] In the other mechanism represented by AcrVA2, the Acr interacts with the N terminus of the type V-A effector nuclease Cas12a during translation, resulting in degradation of the template mRNA.[24] While these two examples illustrate that mechanistic steps upstream of RNP effector complex formation can be inhibitory targets of Acrs, the other steps upstream of RNP formation and the many possible mechanisms of inhibition suggest that more paradigms await to be discovered.

In this work, we show that AcrVIB1, the only reported Acr acting against the type VI-B effector nuclease Cas13b,[25] also acts upstream of RNP complex formation but with a unique mechanism of action: promoting rather than inhibiting binding of the crRNA to Cas13b. Binding is unproductive though, preventing processing of the precursor crRNA (pre-crRNA) and blocking induction of collateral RNA cleavage that normally drives cellular dormancy.[26] The bound crRNA is also susceptible to RNase attack, leading to extensive degradation in cells despite being more tightly bound by Cas13b. Finally, cryoelectron microscopy (cryo-EM) structures reveal that the Acr locks Cas13b in a flexible state accessible to partial binding of the crRNA. These findings provide molecular insights into how phages can overcome defense by type VI-B CRISPR-Cas systems and establish a unique anti-CRISPR defense through the conversion of a Cas nuclease from an immune effector into a crRNA sink representing a dead end for the crRNA.

## RESULTS

### AcrVIB1 inhibits collateral RNA cleavage of Cas13b upstream of RNP formation *in vitro*

Our prior experiments using cell-free transcription-translation (TXTL) suggested that AcrVIB1 inhibits RNA collateral cleavage activity of PbuCas13b most strongly when acting prior to RNP complex formation.[25] To explore this observation under fully controlled conditions, we performed collateral RNA cleavage assays *in vitro* using purified components. As part of the assay (Figure 1A), PbuCas13b was combined with either AcrVIB1 or an *in vitro*-transcribed crRNA. After 15 min, the remaining component (AcrVIB1 or crRNA) was added along with target RNA and a collateral RNA substrate linking a fluorophore and a quencher. Fluorescence stemming from separating the fluorophore and quencher through collateral RNA cleavage was then measured over time. As part of the assay, crRNAs with a processed or unprocessed terminal repeat were tested in case the processing state of the crRNAs impacts inhibition by AcrVIB1.

In line with our prior TXTL results,[25] AcrVIB1 exerted a stronger inhibitory effect when added before rather than after the crRNA (Figures 1B and S1). Specifically, AcrVIB1 reduced PbuCas13b's collateral RNA cleavage activity by 97% when added before or 88% when added after a processed crRNA-1 (Figures 1C and S1). A similar trend was observed with two other processed crRNAs, with AcrVIB1 reducing collateral RNA cleavage activity by 94% or 70% (crRNA-2) and by 97% or 23% (crRNA-3) when added before or after the crRNA (Figures 1B, 1C, and S1). These reductions in collateral activities could not be attributed to the 15-min difference in adding the crRNA, as collateral cleavage was similar or even slightly stronger with the delay (Figures 1B and S1). When comparing processed and unprocessed crRNAs, adding the crRNA before rather than after AcrVIB1 resulted in stronger inhibition for the processed vs. unprocessed crRNA (12% vs. 64% for crRNA-1, 30% vs. 41% for crRNA-2, 77% vs. 105% for crRNA-3) (Figures 1C and S1). We attributed stronger inhibition with the unprocessed crRNA to the processed crRNA more readily binding PbuCas13b, which is supported by higher fluorescence output using processed vs. unprocessed crRNAs (Figures 1B and S1). Beyond inhibiting cleavage of the collateral substrate, AcrVIB1 inhibited cleavage of the target RNA (Figure 1D). Overall, AcrVIB1 inhibits both target and collateral RNA cleavage, with the inhibitory step predominantly before RNP complex formation.

### AcrVIB1 destabilizes the crRNA but not Cas13b *in vivo*

After confirming that AcrVIB1 principally inhibits collateral RNA cleavage by PbuCas13b upstream of RNP complex formation, we began exploring the molecular mechanism of inhibition. Prior work on the three Acrs similarly acting upstream of RNP complex formation (AcrIIC2, AcrIIA17, and AcrVA2) served as reference points, with AcrIIC2 and AcrIIA17 leading to crRNA degradation through occlusion from binding Cas9[22,23] and AcrVA2 leading to Cas12a degradation through translational inhibition.[24] As the Acrs led to degradation of the crRNA or the Cas nuclease *in vivo*, we measured crRNA and PbuCas13b abundance when the unprocessed crRNA-1 and PbuCas13b were heterologously expressed along with AcrVIB1 in *E. coli* (Figure 2A).

We first performed western blotting analysis to measure PbuCas13b levels. Co-expressing AcrVIB1 and PbuCas13b led to no difference in the expression or stability of PbuCas13b (Figure 2B), ruling out a mechanism paralleling that of AcrVA2. We therefore turned to northern blotting analysis to measure crRNA levels. Here, both unprocessed and processed crRNA-1 were detectable in the presence of PbuCas13b and in the absence of AcrVIB1 (Figure 2C). In contrast, both crRNA products were greatly diminished in the absence of PbuCas13b as well as in the presence of both PbuCas13b and AcrVIB1. Therefore, PbuCas13b protects the crRNA from turnover, which is reversed in the presence of AcrVIB1.

### AcrVIB1 binds to Cas13b and not to the crRNA

While AcrVIB1 led to destabilization of the crRNA in *E. coli*, AcrVIB1 could be interacting with either PbuCas13b or the crRNA. We therefore measured the extent of binding between AcrVIB1 and either PbuCas13b or the crRNA using microscale thermophoresis (MST) (Figures 3 and S2). As part of the measurements, AcrVIB1 was tracked through its His-tag using a fluorescently tagged-Tris-nitrilotriacetic (NTA) moiety. MST measurements showed tight binding between AcrVIB1 and PbuCas13b, with a calculated dissociation constant ($K_D$) of ~44 nM (Figure 3A). In contrast, MST did not detect any binding between AcrVIB1 and the processed crRNA-1 (Figure 3B). Binding between AcrVIB1 and PbuCas13b was verified by co-immunoprecipitation and mass

Please cite this article in press as: Wandera et al., AcrVIB1 inhibits CRISPR-Cas13b immunity by promoting unproductive crRNA binding accessible to RNase attack, Molecular Cell (2025), https://doi.org/10.1016/j.molcel.2025.01.020



CellPress
OPEN ACCESS

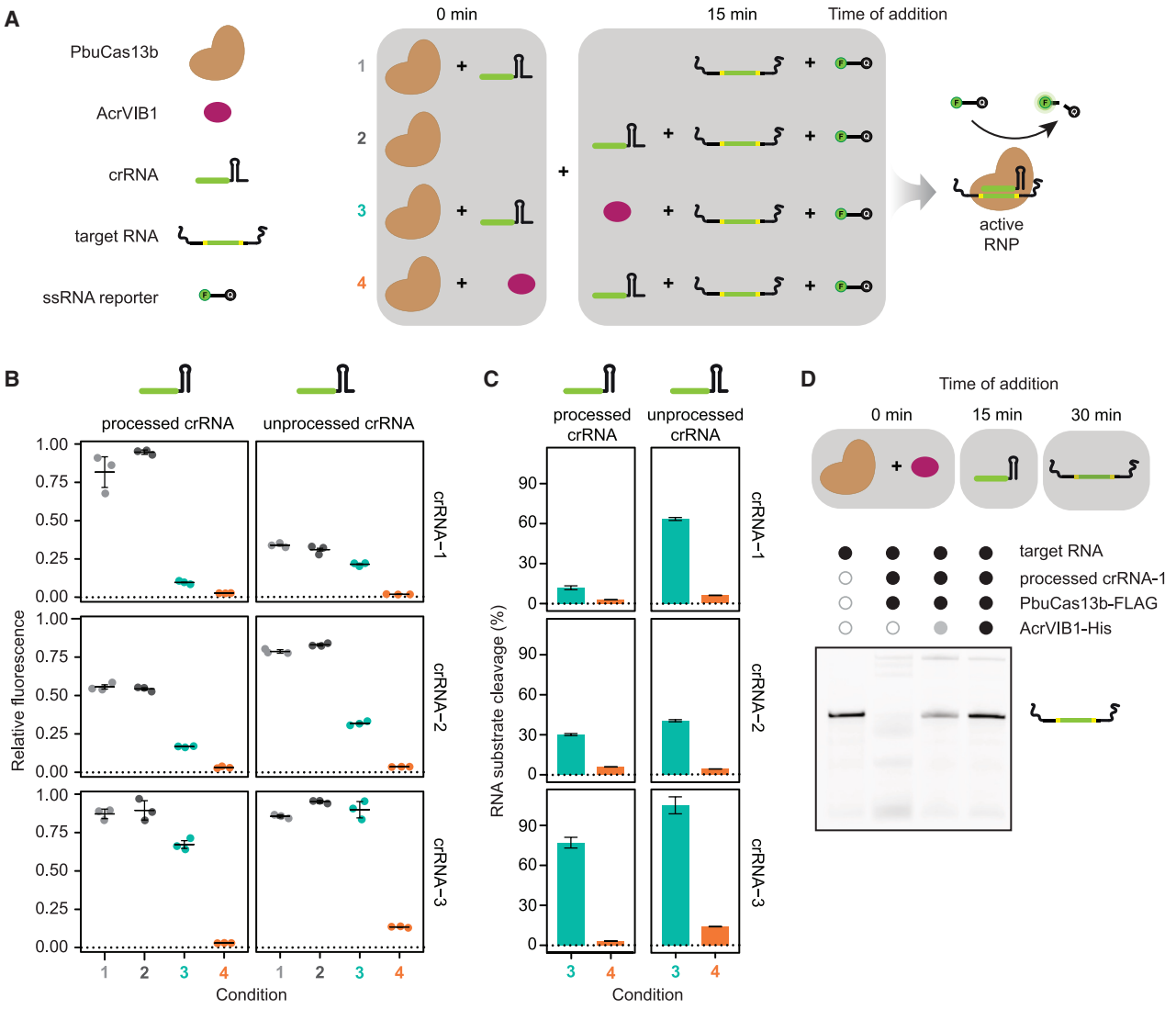



**Figure 1. AcrVIB1 primarily inhibits RNA collateral cleavage by PbuCas13b upstream of RNP formation *in vitro***

(A) Setup of *in vitro* collateral cleavage assay. PbuCas13b was incubated with either a corresponding crRNA or AcrVIB1 for 15 min, before all other components were added. A fluorescently labeled FAM reporter and a target RNA matching the crRNA were always added last. Fluorescence was measured over time, collateral cleavage with values shown at a selected time that ensures that the highest fluorescence signal has not saturated. See Figure S1 for the full time courses. Incubation times are the same for a given crRNA whether processed or unprocessed (2 h for crRNA-1, 5 h for crRNA-2, and 1 h for crRNA-3).

(B) Collateral cleavage activity of Cas13b measured using a set of three crRNAs (crRNA-1–3). Dots represent individual fluorescence measurements, and lines and error bars represent the mean and standard deviation of triplicate independent measurements.

(C) Remaining collateral activity of PbuCas13b calculated using the ratio of fluorescence measurements of conditions with and without AcrVIB1 when crRNA was either added before (3) or after (4) AcrVIB1. Values represent the ratio of the mean of fluorescence measurements and error bars represent the combined standard deviation by calculating the square root of the sum of variances.

(D) Inhibition of RNA target cleavage. Components were added at the indicated time followed by incubation for 60 min. The gel image is representative of two independent experiments.

See also Figure S1.

photometry when both were incubated *in vitro* (Figures S3, S4A, and S4B).

If AcrVIB1 tightly binds and thereby inhibits PbuCas13b while the presence of the crRNA reduces inhibition, then binding of the crRNA to PbuCas13b could negatively affect subsequent interactions with AcrVIB1. To evaluate this possibility directly, we performed MST to measure binding between AcrVIB1 and PbuCas13b already complexed with a crRNA (Figure 3C). In this case, we tracked a crRNA labeled on its 5′ end with a fluorophore, which would not be removed through processing by PbuCas13b.[27] The crRNA rather than AcrVIB1 or PbuCas13b was labeled, as a binding interaction would be registered only if

Please cite this article in press as: Wandera et al., AcrVIB1 inhibits CRISPR-Cas13b immunity by promoting unproductive crRNA binding accessible to RNase attack, Molecular Cell (2025), https://doi.org/10.1016/j.molcel.2025.01.020



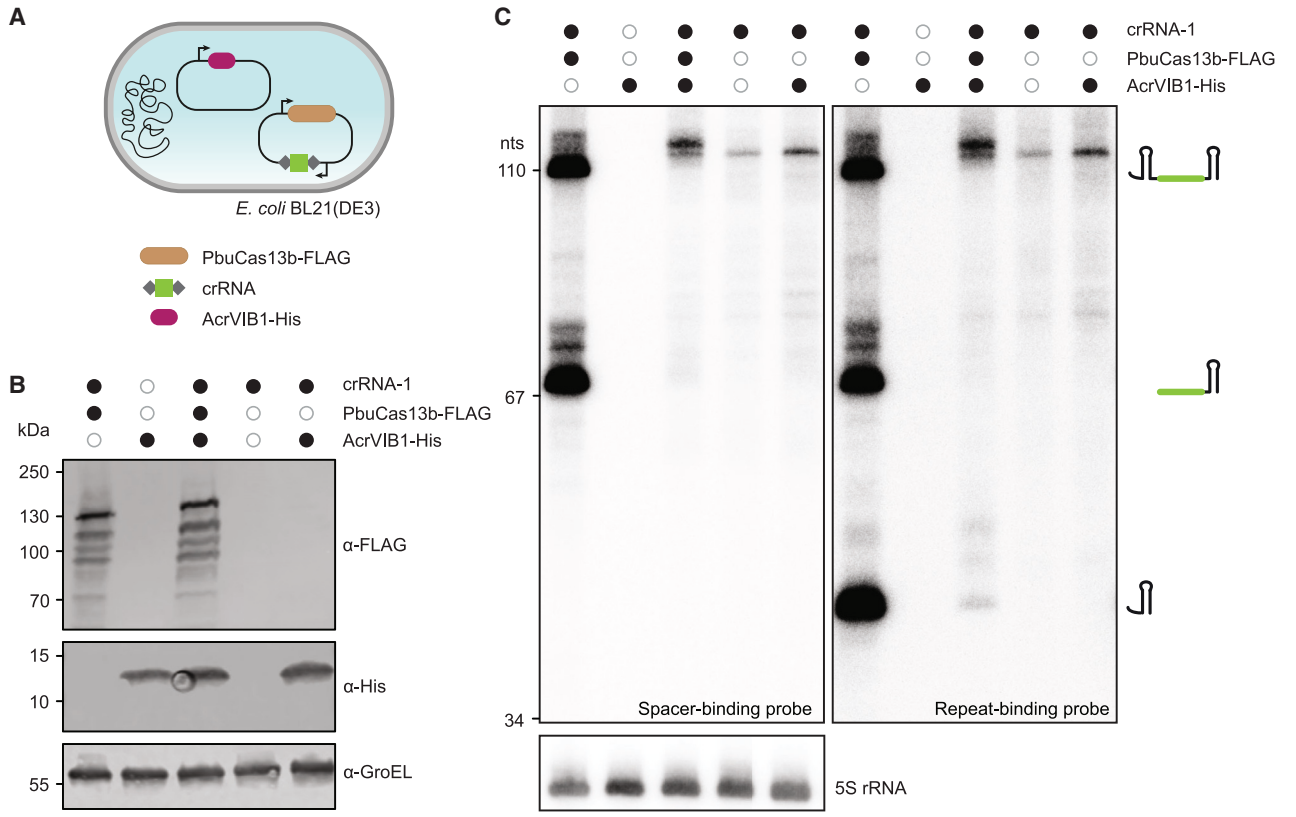



**Figure 2. AcrVIB1 reverses crRNA stabilization by PbuCas13b *in vivo***

(A) Constructs expressing PbuCas13b-FLAG, AcrVIB1-His, and crRNA in *E. coli* BL21(DE3).

(B) Western blotting analysis of PbuCas13b and AcrVIB1. GroEL was detected as a loading control. See also Table S1.

(C) Northern blotting analysis of crRNA using a spacer-hybridizing probe (KW-pr-610) or a repeat-hybridizing probe (KW-pr-725). 5S RNA was detected as a loading control. Gel images in (B) and (C) are representative of three biological replicates.

PbuCas13b bound both the crRNA and AcrVIB1. While no binding of AcrVIB1 was detected under this setup (Figure 3C), mass photometry analysis indicated some interaction between AcrVIB1 and the PbuCas13b:crRNA complex (Figure S4A). This interaction was less stable than that formed when AcrVIB1 is added first based on melting curve determination (Figure S4B). Finally, an electrophoretic mobility shift assay (EMSA) showed that pre-incubating PbuCas13b with a crRNA reduces binding by labeled AcrVIB1 (Figures S4C and S4D). Thus, we can conclude that AcrVIB1 preferentially binds to PbuCas13b rather than the PbuCas13b:crRNA complex, in line with AcrVIB1 inhibiting collateral RNA cleavage by PbuCas13b principally before RNP formation (Figure 1B).

## AcrVIB1 promotes crRNA binding to PbuCas13b

After establishing that AcrVIB1 tightly binds PbuCas13b, we next asked how subsequent binding of the crRNA is affected. Following the precedent set by AcrIIC2 and AcrIIA17,[22,23] we hypothesized that AcrVIB1 occludes crRNA binding, which would explain inhibition prior to RNP formation (Figure 1B) as well as AcrVIB1 yielding crRNA destabilization *in vivo* (Figure 2C). To test this hypothesis, we again applied MST to measure the extent to which the labeled crRNA-1 binds PbuCas13b already complexed with AcrVIB1 (Figures 3D, 3E, and S2). Surprisingly, the crRNA bound significantly tighter in the presence rather than in the absence of AcrVIB1, with respective $K_D$ values of ~160 nM and ~1 μM (Figures 3D and 3E) ($p$ = 0.032). We obtained similar results by EMSA, where crRNA binding to PbuCas13b required a high (200 nM) concentration of the nuclease and was enhanced when PbuCas13b was pre-incubated with AcrVIB1 (Figure S4E). While these binding affinities were low compared with the picomolar affinities measured between guide RNAs and the *S. pyogenes* Cas9,[28] such affinities have been rarely measured and could vary widely across Cas single effector nucleases (Figure 1B). Overall, in stark contrast to AcrIIC2 and AcrIIA17, AcrVIB1 enhances rather than occludes crRNA binding.

## The bound crRNA is not processed and yields altered target RNA binding

While AcrVIB1 promotes crRNA binding to PbuCas13b, the resulting complex exhibits greatly reduced target-dependent target and collateral RNA cleavage (Figures 1B and 1D). We therefore evaluated the impact of AcrVIB1 binding on two intermediate steps between crRNA binding and collateral RNA cleavage: crRNA processing and target RNA binding. Beginning with

Please cite this article in press as: Wandera et al., AcrVIB1 inhibits CRISPR-Cas13b immunity by promoting unproductive crRNA binding accessible to RNase attack, Molecular Cell (2025), https://doi.org/10.1016/j.molcel.2025.01.020



CellPress
OPEN ACCESS

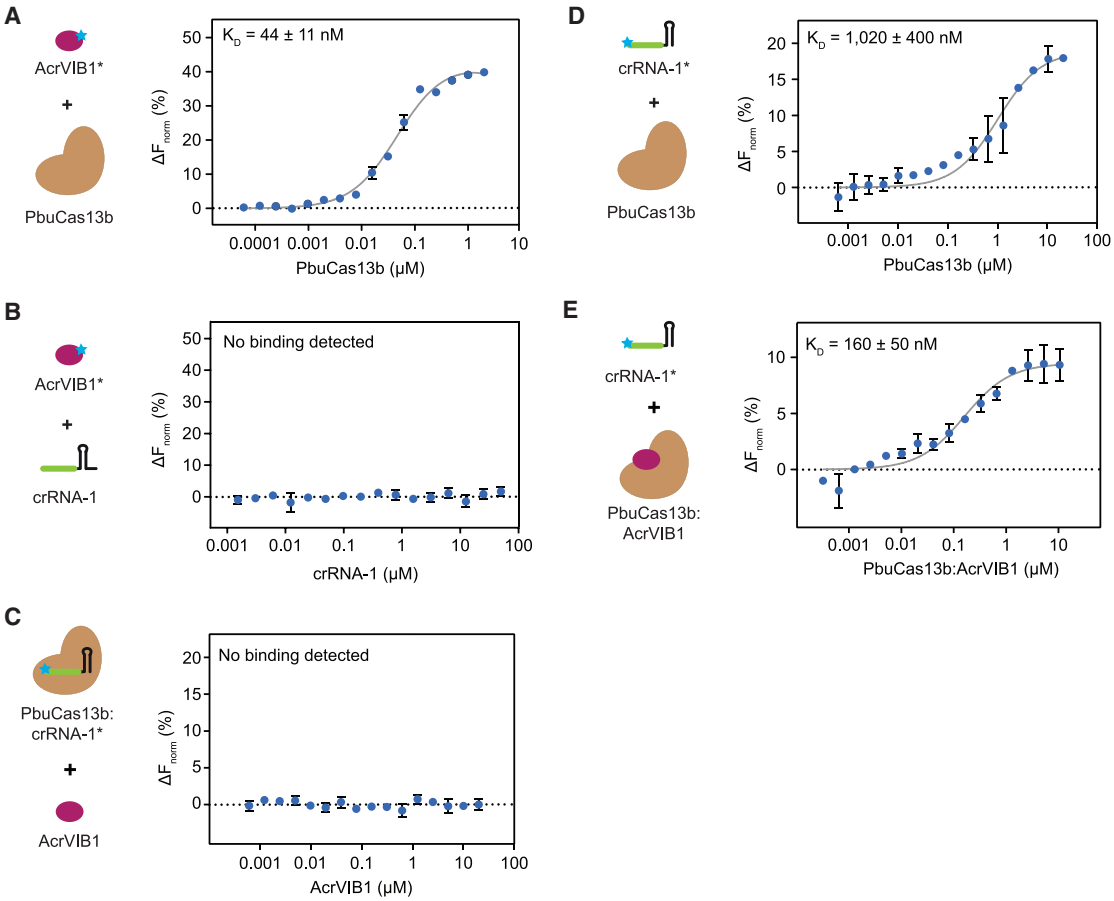



**Figure 3. AcrVIB1 promotes crRNA binding by directly interacting with PbuCas13b**

(A–E) MST assay to quantify interactions between (A) PbuCas13b and His-tag-labeled AcrVIB1, (B) crRNA and His-tag-labeled AcrVIB1, (C) AcrVIB1 and the PbuCas13b:crRNA complex, with 5′-labeled crRNA, (D) PbuCas13b and 5′-labeled crRNA and (E) the PbuCas13b:AcrVIB1 complex and 5′-labeled crRNA. In all experiments, the labeled component is indicated by an asterisk. Dots represent the movement of the molecules at a specific concentration in response to a temperature gradient. Error bars depict the standard deviation of triplicate independent measurements. The corresponding MST traces can be found in Figures S3A–S3E. The binding affinities for the crRNA to PbuCas13b (D) and to PbuCas13b:AcrVIB1 (E) are significantly different ($p$ = 0.032).
See also Figures S2–S4.

crRNA processing, we incubated a 3′-labeled crRNA-1 with a full-length terminal repeat and downstream truncated spacer with PbuCas13b alone or already in complex with AcrVIB1 (Figure 4A). While PbuCas13b alone fully processed the crRNA, PbuCas13b complexed with AcrVIB1 could no longer process the crRNA, especially at higher concentrations of AcrVIB1. The crRNA also remained intact in the presence of AcrVIB1, ruling out any degradation directly mediated by the Acr or the AcrVIB1-bound Cas13b. Thus, AcrVIB1's interaction with Cas13b prevents crRNA processing.

While inhibition of crRNA processing suggests disruption of other downstream steps, crRNA processing in itself is not necessary for Cas13b to recognize its target RNAs and activate collateral RNA cleavage.[29] We therefore evaluated the second intermediate step, target RNA binding (Figures 4B and 4C). We again used MST, where we tracked the target RNA using a 5′-label. We also used a buffer that chelates free magnesium ions to allow target RNA binding without the confounding effect of collateral RNA cleavage, paralleling prior work on Cas13b.[30] Under these conditions, pre-incubating PbuCas13b with AcrVIB1 resulted in modestly but significantly reduced target RNA binding by the PbuCas13b:crRNA-1 RNP complex from a K$_D$ of 85 to 153 nM ($p$ = 0.047). The K$_D$ value in the absence of AcrVIB1 paralleled those reported previously (27–42 nM).[30] Performing a similar assay via EMSA revealed a distinct banding pattern for bound target RNA, suggesting that the interaction between PbuCas13b:crRNA and the target RNA is altered in the presence of AcrVIB1 (Figure S5A). Similar changes in banding patterns for the bound target RNA as well as reduced target RNA binding in the presence of AcrVIB1 were observed via EMSA using crRNA-2 and crRNA-3 (Figures S5B and S5C). Between disruption of crRNA processing and altered target RNA recognition, the enhanced binding of crRNA to the PbuCas13b:AcrVIB1 can be considered unproductive.

Please cite this article in press as: Wandera et al., AcrVIB1 inhibits CRISPR-Cas13b immunity by promoting unproductive crRNA binding accessible to RNase attack, Molecular Cell (2025), https://doi.org/10.1016/j.molcel.2025.01.020



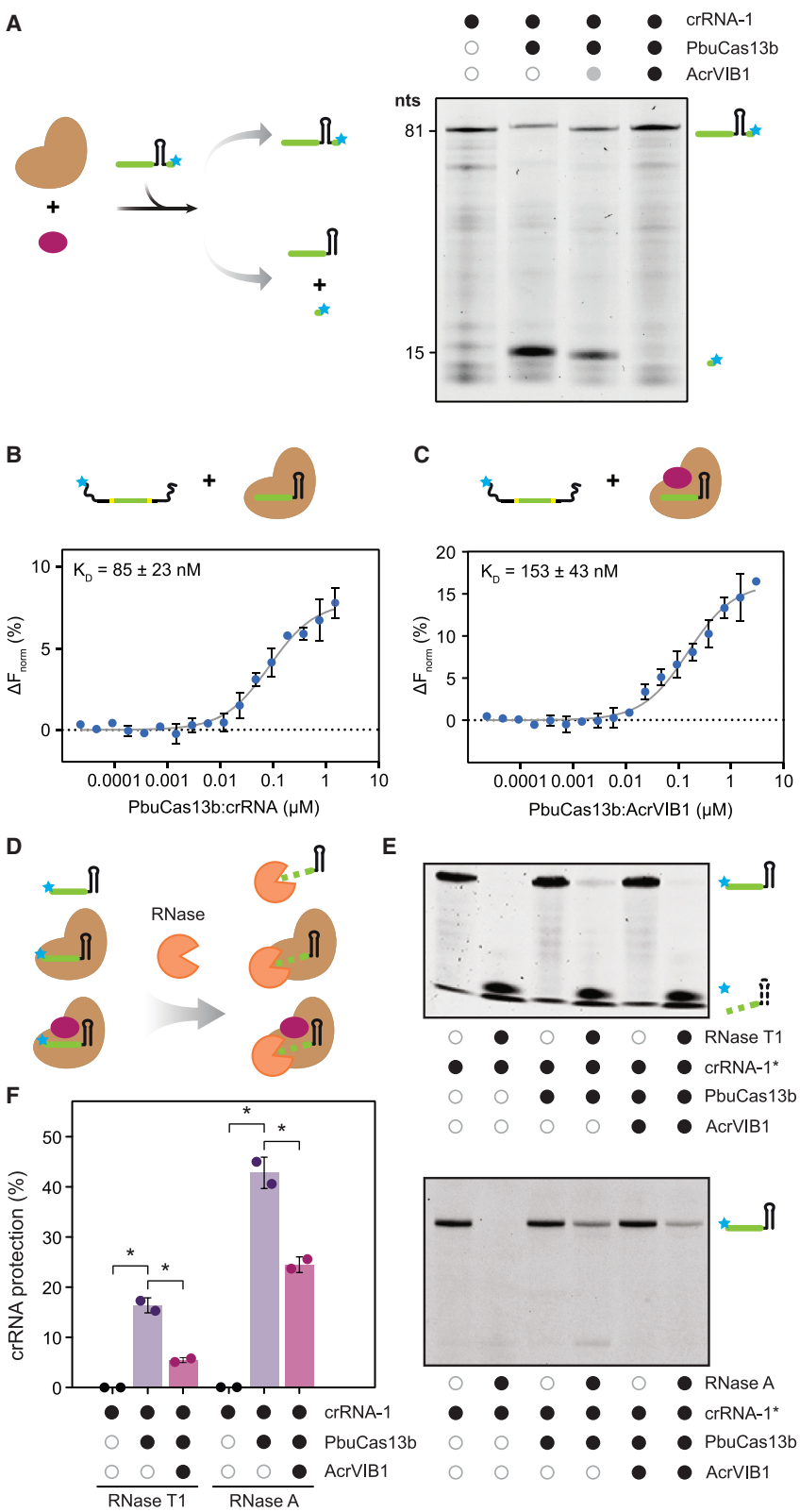



**Figure 4. AcrVIB1 fully inhibits crRNA processing, partially inhibits target RNA binding, and facilitates crRNA degradation by an RNase even in the presence of PbuCas13b**

(A) Assessing crRNA processing by PbuCas13b in absence or presence of AcrVIB1. AcrVIB1 was added in two concentrations indicated by the filled gray (100 nM) and black (1,000 nM) circle. The gel image is representative of two independent replicates.

(B) MST assay to quantify interactions between the PbuCas13b:crRNA complex and a 5′-labeled target RNA.

(C) MST assay to quantify interactions between the PbuCas13b:AcrVIB1:crRNA complex and a 5′-labeled target RNA. Buffer conditions allowed binding yet prevented cleavage of target RNA to prevent RNA turnover that could distort the measured $K_D$ (see STAR Methods). Dots represent the movement of the molecules at a specific concentration in response to a temperature gradient. Error bars depict the standard deviation of triplicate independent measurements. The MST traces corresponding to (B) and (C) can be found in Figures S3F and S3G. The binding affinities of the target RNA to PbuCas13b:crRNA and to PbuCas13b:AcrVIB1:crRNA are significantly different ($p = 0.047$).

(D) Setup of the *in vitro* RNase degradation assay exposing PbuCas13b, AcrVIB1, and crRNA-1 to RNase T1 or RNase A.

(E) PAGE analysis of 5′-labeled crRNA subjected to the RNase degradation assay. Each gel image is representative of two independent replicates.

(F) Analysis of the gel image shown in (B), using the difference of the bands between samples with and without exposure to RNase T1 or RNase A to calculate the extent of crRNA protection. * $p < 0.05$. See also Figures S2, S4, and S5.

Please cite this article in press as: Wandera et al., AcrVIB1 inhibits CRISPR-Cas13b immunity by promoting unproductive crRNA binding accessible to RNase attack, Molecular Cell (2025), https://doi.org/10.1016/j.molcel.2025.01.020



CellPress
OPEN ACCESS

## The presence of AcrVIB1 exposes the Cas13b-bound crRNA to RNase attack

We showed that AcrVIB1's interaction with PbuCa13b leads to unproductive crRNA binding that prevents crRNA processing, alters target RNA binding, and stymies target-dependent collateral RNA cleavage. What remains unclear though is how these mechanisms would reduce crRNA stability *in vivo* (Figure 2C), as enhanced crRNA binding to PbuCas13b in the presence of AcrVIB1 would be expected to lead to greater protection of the crRNA against host RNases. We therefore hypothesized that unproductive crRNA binding renders the bound crRNA accessible to RNases, leading to crRNA turnover *in vivo* even in the presence of Cas13b.

To test this hypothesis, we exposed crRNA-1 to RNase T1, an endoribonuclease that cleaves after guanine nucleotides in single-stranded RNA, or RNase A, an endoribonuclease that cleaves after cytidine and uracil residues, in the presence or absence of PbuCas13b and AcrVIB1 (Figure 4D). The crRNA alone was completely degraded by both RNases under our testing conditions (Figure 4E). The presence of PbuCas13b significantly albeit partially protected the crRNA from RNase T1 (Figures 4E and 4F), where we attribute incomplete protection to the poor binding affinity between PbuCas13b and the crRNA (Figure 3D) that would lead to regular crRNA release. In the presence of PbuCas13b and AcrVIB1, protection significantly dropped compared with no RNase (Figures 4E and 4F), even though more crRNA would be bound to PbuCas13b. We therefore conclude that the crRNA is more prone to RNase degradation in the presence of AcrVIB1, explaining crRNA destabilization *in vivo* despite the Acr enhancing binding of the crRNA to PbuCas13b.

## AcrVIB1 prevents Cas13b from closing around the crRNA

AcrVIB1 blocks crRNA processing and activation of collateral cleavage yet has a more subtle effect on target RNA binding, suggesting that the Acr exerts structural effects on PbuCas13b that impede the nuclease's ability to perform different functions. We therefore determined cryo-EM structures of PbuCas13b bound to a crRNA in the absence or presence of AcrVIB1 (Figure 5). When Acr was omitted, we observed a single compact structure that could be refined to 3.1 Å resolution (Figure 5A) and that paralleled the previously published crystallized PubCas13b:crRNA complex (PDB: 6DTD).[31] Briefly, PbuCas13b adopts a heart-shaped conformation in which two higher eukaryotes and prokaryotes nucleotide binding (HEPN) domains (HEPN-1 and HEPN-2), located at the N- and C terminus of the protein, form the apex containing the Cas13b nuclease active site, whereas two helical domains (helical-1 and helical-2) together with a lid-structure establish a solvent-accessible chamber that binds the 3′ stem-loop and leaves room for the unpaired 5′-stretch of the crRNA as well as for parts of the target RNA. Importantly, in this complex, the stem-loop of the crRNA is clamped tightly between the helical-1 and helical-2 domains, which sit on top of the HEPN-2 and HEPN-1 domains, respectively, and also contact the lid. Consequently, the crRNA cannot leave the complex without structural rearrangements of the protein, implying that PbuCas13b adopts a more open conformation to load the crRNA.

Building on prior observations garnered from the crystal structure,[31] parts of the crRNA repeat become visible in the cryo-EM structure, supporting the prior hypothesis that this stretch leaves the chamber through the large opening located at the face opposite to the HEPN active site of PbuCas13b (Figure 5A).

Including AcrVIB1 with PbuCas13b and the crRNA led to heterogeneous and less compact particles. The only trackable conformation in these samples could be refined to an overall resolution of 4.2 Å (Figure 5B). While the quality of the resulting map does not reveal individual secondary structure elements, it clearly shows that the helical-2 domain has lost its contact to HEPN-1 and the lid domains, leading to a swing-out motion of ~60 Å at its tip. As a consequence, the crRNA is now fully solvent-exposed, and its 3′ end points away from the core of the Cas13b nuclease and into the direction of the swung-out helical-2 domain (Figure 5B).

## AcrVIB1 binds the helical-2 domain of Cas13b that prevents the crRNA from being secured

Because this opening of the Cas13b:crRNA complex occurs in the presence of AcrVIB1, it is conceivable that the Acr must be bound to the complex, thereby preventing its role as a clamp protecting and holding the crRNA in place. However, the exact position of AcrVIB1 was not obvious in the cryo-EM map because of its low resolution. While considering different possible locations, we noticed that the density around the shifted helical-2 domain was less resolved than for the remainder of the protein. The lower resolution may be a consequence of local flexibility, capturing conformations with different degrees of opening in the map. Alternatively, the lower resolution could indicate binding of AcrVIB1 to the helical-2 domain.

With the recent advent of AlphaFold3,[32] we explored whether AcrVIB1 interacts with the helical-2 domain or elsewhere on PbuCas13b. As calculations with the complete nuclease and AcrVIB1 were inconclusive, we modeled a complex of AcrVIB1 only with the helical-2 domain. In contrast to similar approaches with the predecessor software AlphaFold2,[33] the more recent version resulted in a reproducible high-confidence model of a 1:1 complex (Figure 6A). When this model is mapped to the open conformation of the Cas13b:crRNA complex, AcrVIB1 wedges between the lid and the helical-2 domain (Figure 6B). Importantly, when the helical-2:AcrVIB1 model is superimposed onto the closed conformation of PbuCas13b, AcrVIB1 would arrive at the inner RNA-binding cavity and lead to severe clashes with parts of the nuclease, explaining why AcrVIB1 does not bind to the pre-formed PbuCas13b:crRNA complex in our experiments. On the other hand, the open conformation is expected to allow the crRNA to more easily access its binding site in PbuCas13b, which could explain why AcrVIB1 strengthens crRNA binding. At the same time, the crRNA remains unprotected in this complex, making it prone to degradation by RNases as we observed experimentally (Figures 4D–4F). The inability of the helicase-2 domain to close around the crRNA likely prevents further conformational changes previously hypothesized as necessary steps to activate collateral RNA cleavage.[31]

To validate the AlphaFold3 model experimentally, we produced the helical-2 domain recombinantly and assessed

Please cite this article in press as: Wandera et al., AcrVIB1 inhibits CRISPR-Cas13b immunity by promoting unproductive crRNA binding accessible to RNase attack, Molecular Cell (2025), https://doi.org/10.1016/j.molcel.2025.01.020



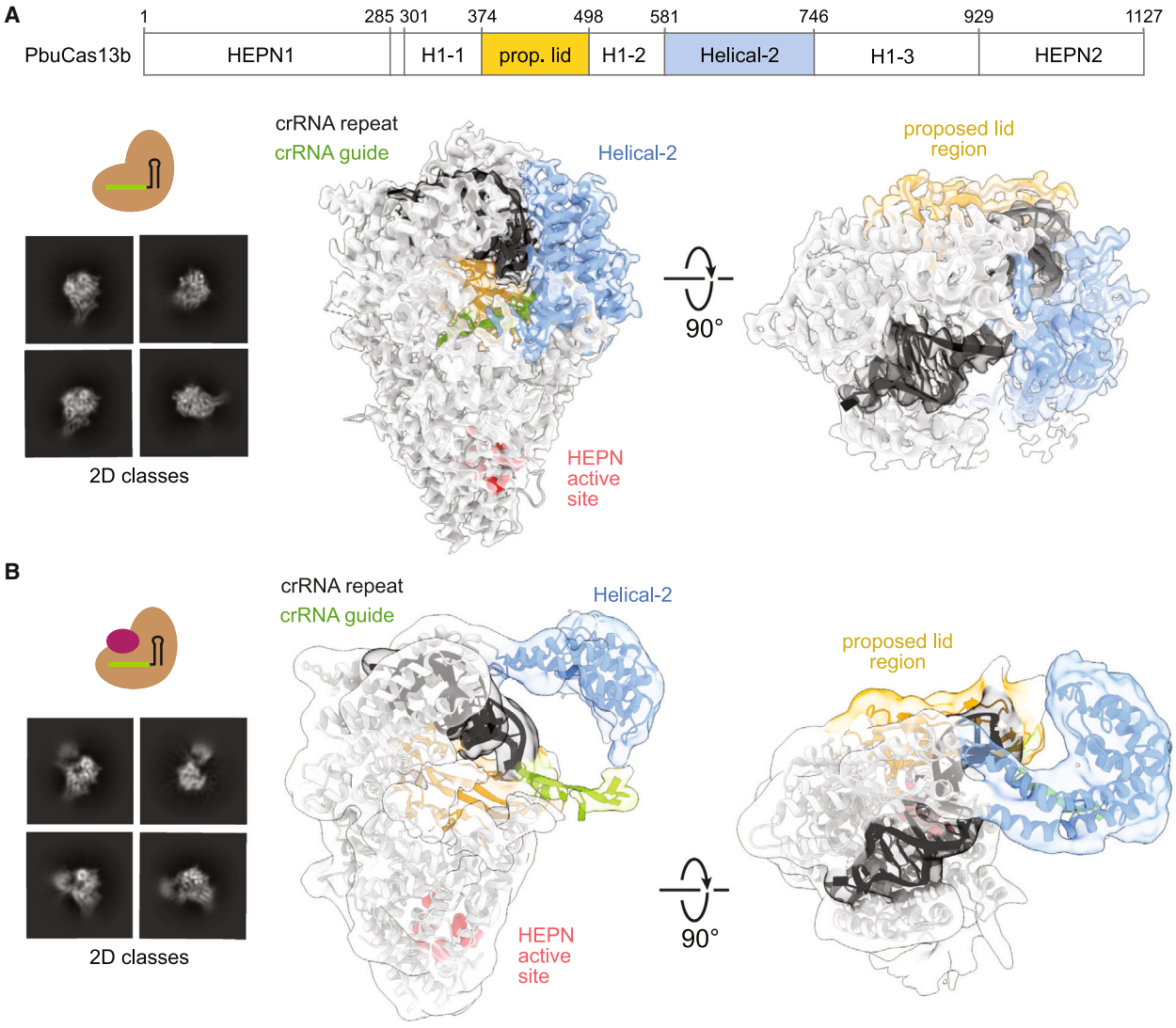



**Figure 5. The presence of AcrVIB1 untethers the helical-2 domain of PbuCas13b, exposing the bound crRNA**

(A) Cryo-EM structure of PbuCas13b with bound crRNA. The structure (9FCV) has an average resolution of 3.09 Å. The cryo-EM map is colored according to the linear domain organization of PbuCas13b reported previously.[31] The crRNA is colored in green (guide) and black (repeat), and conserved residues of the HEPN active site are colored in light red. Representative 2D classes of cryo-EM particles are displayed on the left.

(B) PbuCas13b:crRNA complex in an open conformation observed in the presence of AcrVIB1. The model was obtained by morphing of the structure shown in (A) into a 4.23 Å resolution map. Representative 2D classes of cryo-EM particles are displayed on the left.

complex formation with AcrVIB1 by size exclusion chromatography with multi angle light scattering (SEC-MALS) and Spectral Shift titration. This analysis revealed a 1:1 complex of the expected molecular mass (Figure 6C), with a dissociation constant of 251 nM (Figure 6D). While the recombinant complex was recalcitrant to crystallization, we could corroborate the overall shape and position of the predicted secondary structure elements with a low-resolution cryo-EM reconstruction of the 34-kDa helical-2:AcrVIB1 particle (Figures 6E and 6F).

To probe the importance of residues in the predicted interface between PbuCas13b and AcrVIB1 (Figure S6A), we tested associated amino-acid substitutions in both PbuCas13b and AcrVIB1 using our previously reported TXTL assay.[25] The assay reads out nuclease activity through silencing of a targeted GFP transcript, which is reversed through inhibition by the expressed AcrVIB1 (Figure S6B). Of the three tested substitutions in PbuCas13b (K627A, N634A, and R662A) and AcrVIB1 (D37A/D38A, S56A, and T70A), R662A in PbuCas13b as well as D37A/D38A and T70A in AcrVIB1 mediated a substantial reversal of inhibition (Figures S6C and S6D). The attenuated inhibition supports the predicted interactions between AcrVIB1 and the helical-2 domain of PbuCas13b, while the lack of inhibition at the other tested residues could reflect multisite interactions that collectively contribute to binding and inhibition.

As an additional means to probe-binding interactions, we evaluated the *Riemerella anatipestifer* (Ran)Cas13b, which shares

Please cite this article in press as: Wandera et al., AcrVIB1 inhibits CRISPR-Cas13b immunity by promoting unproductive crRNA binding accessible to RNase attack, Molecular Cell (2025), https://doi.org/10.1016/j.molcel.2025.01.020



CellPress
OPEN ACCESS

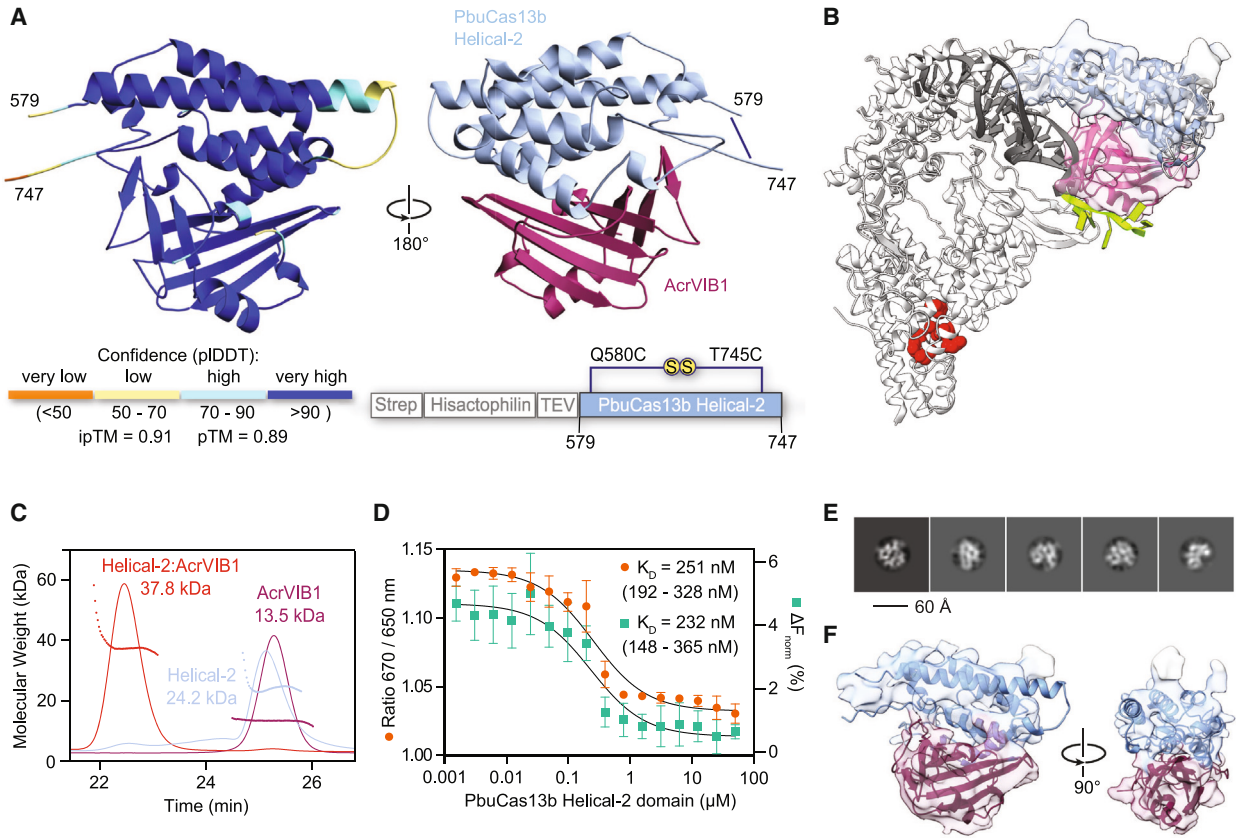



**Figure 6. AcrVIB1 binds the helical-2 domain of PbuCas13b**

(A) AlphaFold3 model of the PbuCas13b helical-2 domain (residues 579–747) bound to AcrVIB1. Left: structure colored according to the modeling confidence (predicted local distance difference test [pLDDT] score). Right: 180° rotation of the model and colored to indicate AcrVIB1 (violet) and the helical-2 domain (blue). A dark blue line indicates the position of an artificial disulfide bond that was introduced for stabilization of the isolated helical-2 domain.

(B) Full-length PbuCas13b (light gray) with bound cRNA (repeat in dark gray, guide in green) and an open and extended helical-2 domain superposed with the cryo-EM complex shown in (F). AcrVIB1 is colored in violet, the PbuCas13b helical-2 domain is colored in blue, and the HEPN active site is colored in red.

(C) SEC-MALS profiles of AcrVIB1 (violet), the PbuCas13b helical-2 domain (blue), and the complex of both (red). The obtained molecular weights are in good agreement with the expected values (AcrVIB1: 13.6 kDa, PbuCas13b helical-2 domain: 20.4 kDa, complex: 34.0 kDa). Results are representative of duplicate independent runs.

(D) Binding-affinity measurements of the PbuCas13b helical-2 domain to fluorescently labeled AcrVIB1. Orange dots: analysis based on the 670/650 nm emission ratio of the fluorescent dye. Teal squares: analysis of the same samples based on MST. Dots/squares and error bars represent the mean and SD of 4 independent replicates.

(E) Representative 2D classes of the 34-kDa complex comprising PbuCas13b helical-2 domain (residues 579–747) and AcrVIB1.

(F) Superposition of the AlphaFold3 model from (A) with the 34-kDa AcrVIB1:PbuCas13b helical-2 domain (residues 579–747) complex. The resulting map has a resolution of 5.11 Å.

See also Figure S6.

43% identity with PbuCas13b. RanCas13b and AcrVIB1 coexist in the same *R. anatipestifer* genome, although AcrVIB1 poorly inhibits this Cas13b.[25] We hypothesized that the few amino-acid differences within the implicated portion of the helical-2 domain prevents inhibition by AcrVIB1 (Figure S6E). Substituting four residues in RanCas13b to match the aligned residue in PbuCas13b (K559N, Y609K, W627R, and R630Q), we found that one substitution (R630Q) substantially enhanced inhibition by AcrVIB1 in the TXTL assay (Figure S6F). Sequence divergences in this region of the helical-2 domain thus appear to limit the host range of AcrVIB1. Overall, our mutational analyses help corroborate AcrVIB1 directly binding to the helical-2 domain of PbuCas13b.

## DISCUSSION

Based on our collective results, we propose a detailed model governing the mechanism of action of AcrVIB1, the only known inhibitor of a Cas13b nuclease (Figure 7). In the absence of the Acr, Cas13b binds and processes the pre-crRNA, after which target RNA can be recognized to activate collateral RNA cleavage. In the presence of the Acr, AcrVIB1 tightly binds Cas13b through the helical-2 domain, thereby locking Cas13b in an open conformation that more readily allows binding of a pre-crRNA. pre-crRNA binding is unproductive though, preventing pre-crRNA processing. The guide portion of the crRNA remains free to hybridize to the target RNA, albeit with slightly reduced

Please cite this article in press as: Wandera et al., AcrVIB1 inhibits CRISPR-Cas13b immunity by promoting unproductive crRNA binding accessible to RNase attack, Molecular Cell (2025), https://doi.org/10.1016/j.molcel.2025.01.020



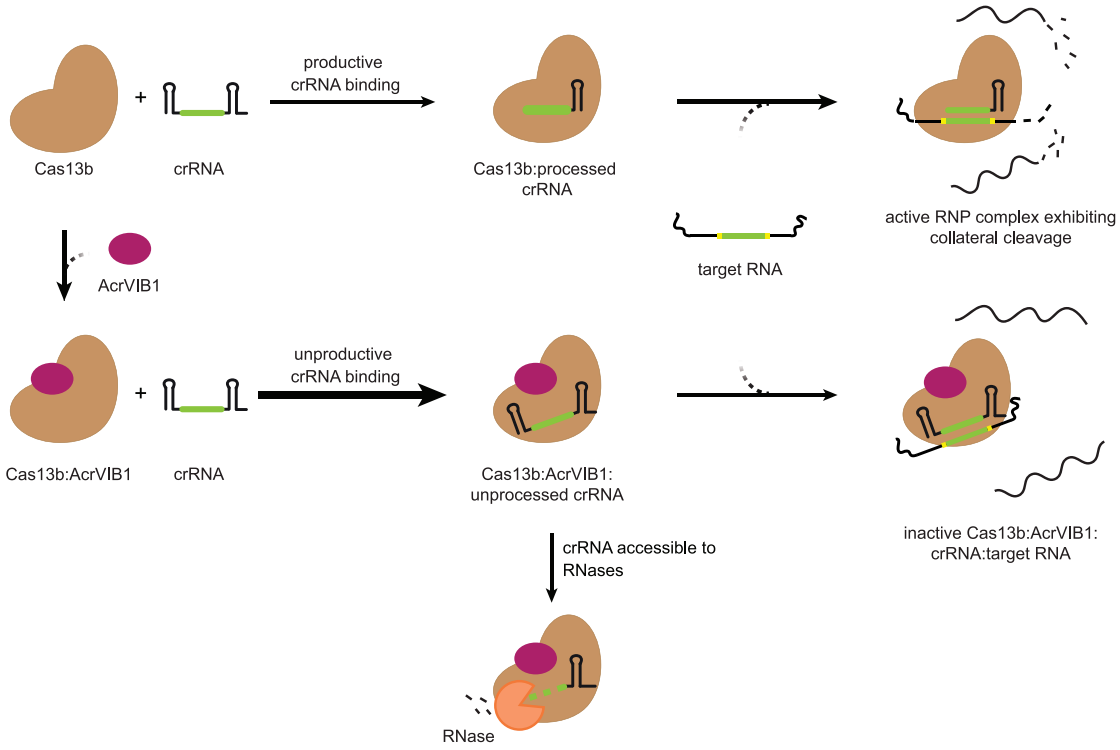



**Figure 7. Proposed model for inhibition of Cas13b-based immunity by AcrVIB1**

Cas13b weakly binds to a crRNA to form an RNP complex followed by crRNA processing. The RNP complex can then recognize a target RNA that activates collateral RNA cleavage. AcrVIB1 binds to Cas13b, leading to stronger crRNA binding to the Cas13b:AcrVIB1 complex. The bound crRNA does not undergo processing but can still hybridize to the target RNA. However, target RNA hybridization does not activate collateral RNA cleavage. The crRNA bound to Cas13b is protected from RNases, while the crRNA bound to the Cas13b:AcrVIB1 complex is susceptible to attack by cellular RNases.

affinity. However, even with target RNA hybridization, the AcrVIB1-bound Cas13b cannot undergo the structural changes predicted to align the HEPN domains necessary for collateral RNA cleavage.[31] Because the bound crRNA is not fully secured, it becomes accessible to RNases that at least partially degrade the crRNA. If the degraded crRNA is released, the Cas13b:AcrVIB1 complex could subsequently bind but not protect additional crRNA molecules, effectively turning Cas13b into a crRNA sink. In total, AcrVIB1 blocks immune activation of Cas13b in the presence of a target RNA. If a crRNA is already bound to Cas13b, then AcrVIB1 loses its ability to inhibit immune activation because the binding surface on the helical-2 domain is buried in the Cas13b:crRNA complex.

Apart from supporting the proposed inhibitory mechanism of AcrVIB1, the cryo-EM analyses shed light on the crRNA loading step of Cas13b. This step has previously remained obscure due to the fact that only two crystal structures of Cas13b:crRNA complexes are currently available, and these structures do not provide direct evidence for interdomain flexibility within Cas13b nucleases.[31,34] Binding of AcrVIB1 revealed an alternative conformation in which the helical-2 domain remains in a swung-out conformation. As this domain directly interacts with the crRNA in the Cas13b:crRNA structures, we propose that it opens to accommodate crRNA binding. It is conceivable that the same domain also moves to accommodate complete hybridization between the crRNA and target RNA, although the previously proposed lid domain could also serve this function.[31] Thus, there are still many features of Cas13b activation that remain unclear, such as how target recognition leads to nuclease activation. Further studies with AcrVIB1 could help dissect these steps.

The elucidated mechanism of action represents a distinct entry into the short but diverse list of known Acrs acting upstream of RNP formation. Among already known mechanisms are the degradation of effector protein mRNA and the occlusion of crRNAs to prevent RNP complex formation.[22–24] Separate from Acrs, RNA-based anti-CRISPR elements called Racrs were recently shown to act upstream of RNP formation by mimicking crRNA repeats that form non-functional RNPs.[35] AcrVIB1 introduces a distinct mechanism to this list by promoting rather than occluding crRNA binding but in a way that blocks target-dependent activation and leads to crRNA degradation *in vivo*. At most, this mechanism resembles that of AcrVA1, which cleaves the guide region of a Cas12a crRNA.[36] However, AcrVA1 only cleaves the crRNA within the formed RNP, whereas AcrVIB1 promotes the formation of a non-functional RNP. Given the diverse mechanisms exhibited by AcrVIB1 and these few other Acrs and Racrs, additional Acrs likely await discovery. For instance, these hypothetical Acrs could act through similar mechanisms against other Cas nucleases besides Cas13b or

Please cite this article in press as: Wandera et al., AcrVIB1 inhibits CRISPR-Cas13b immunity by promoting unproductive crRNA binding accessible to RNase attack, Molecular Cell (2025), https://doi.org/10.1016/j.molcel.2025.01.020



CellPress
OPEN ACCESS

**Table 1. Cryo-EM data collection, structure refinement, and validation statistics**

| Data collection and processing | PbuCas13b:crRNA complex (PDB: 9FCV, EMDB: EMD-50322) | AcrVIB1:PbuCas13b:crRNA complex (EMDB: EMD-51509) | AcrVIB1/PbuCas13b Helical-2 domain (EMDB: EMD-51513) |
|---|---|---|---|
| Magnification | 130,000 | 130,000 | 130,000 |
| Voltage (kV) | 200 | 200 | 200 |
| Electron exposure ($e^{-}$/Å$^2$) | 40 | 40 | 60 |
| Defocus range (μm) | −0.6 to −2.0 | −0.6 to −2.00 | −0.6 to −1.6 |
| Pixel size (Å) | 0.91 | 0.91 | 0.91 |
| Symmetry imposed | C1 | C1 | C1 |
| Image stacks (no.) | 3,778 | 10,707 | 8,206 |
| Initial particle images (no.) | 1,903,944 | 1,250,433 | 7,229,692 |
| Final particle images (no.) | 356,629 | 120,153 | 1,078,020 |
| Map resolution (Å) | 3.09 | 4.23 | 5.11 |
| FSC threshold | 0.143 | 0.143 | 0.143 |
| Refinement | | | |
| No. of protein residues | 1,057 | – | – |
| No. of rna bases | 44 | – | – |
| No. of atoms | 19,225 | – | – |
| Root-mean-square deviations (RMSDs) | | | |
| Bond lengths (Å) | 0.002 | – | – |
| Bond angles (°) | 0.404 | – | – |
| PDB validation | | | |
| Clash score | 2.34 | – | – |
| Poor rotamers (%) | 0.00 | – | – |
| C-beta deviation | 0.00 | – | – |
| Ramachandran plot | | | |
| Favored (%) | 97.7 | – | – |
| Allowed (%) | 2.2 | – | – |
| Disallowed (%) | 0.1 | – | – |

act at other steps upstream of RNP formation, such as transcription of the Cas nuclease or pre-crRNA, crRNA processing by host factors such as RNase III or RNase E, or as part of spacer acquisition.

Given that AcrVIB1 and these other examples would not be effective after the RNP effector complex is formed, it raises the question: under which infection conditions do these examples help circumvent CRISPR-based immunity? Inhibition would be unlikely to benefit an initial infection by an Acr-encoding phage, as the expressed Acr (or Racr) would not inhibit pre-formed RNP complexes surveilling for the invading phage genome. Instead, these Acrs could assist with a follow-on wave of phage infections, an altruistic effect also associated with Acrs inhibiting some DNA-targeting CRISPR-Cas systems.[37,38] If the phage contains a mutated target site but the site could drive priming,[39,40] then Acrs acting upstream of RNP formation could inhibit CRISPR immunity before a new spacer can be acquired and produce a matching crRNA. As Acrs are often found together in anti-defense islands, multiple mechanisms of inhibition acting upstream of and on RNP complex formation could also yield more robust anti-defense under different infection conditions. Overall, more work exploring the ramifications of different inhibitory mechanisms of Acrs under different infection conditions could shed further light on the bacterial-phage arms race.

One notable observation while elucidating AcrVIB1's mechanism of action is the poorer binding affinity between PbuCa13b and its crRNA, at least compared with that measured for SpyCas9.[28] We still observe collateral RNA cleavage activity, so the low binding affinity between PbuCas13b and crRNA does not compromise RNP activation. This observation raises the question of how variable binding affinities can be between Cas effector nucleases and their crRNAs and their potential consequences on CRISPR immunity. In the case of Cas13b and AcrVIB1, we speculate that the poor binding affinity grants AcrVIB1 an opportunity to inhibit Cas13b before a crRNA is bound; otherwise, AcrVIB1 would be rendered ineffective both to bind Cas13b and serve as a crRNA sink.

Beyond its relevance to bacterial-phage interactions, the identification and characterization of AcrVIB1 lays the foundation for its use for controlling Cas13-based functions. Indeed, Cas13 nucleases have been adapted for a number of RNA-centric applications, including post-transcriptional silencing, RNA editing, molecular diagnostics, and *in vivo* imaging.[41–44] Currently, there are only a limited number of Acrs that inhibit type VI CRISPR-Cas systems, and only one published application using the Acr for

Please cite this article in press as: Wandera et al., AcrVIB1 inhibits CRISPR-Cas13b immunity by promoting unproductive crRNA binding accessible to RNase attack, Molecular Cell (2025), https://doi.org/10.1016/j.molcel.2025.01.020



phage engineering.[45] In this context, the Cas13a inhibitor AcrVIA1 is introduced as a selection marker via homologous recombination, together with a gene of interest.[17] Only phages carrying the gene of interest and AcrVIA1 would survive Cas13a targeting due to the inhibitory activity of AcrVIA1 against Cas13a.[45] As AcrVIB1 acts prior to RNP complex formation, applications that rely on a pre-formed RNP complex would be less suitable, such as phage engineering or molecular diagnostics. However, there are other applications in which an RNP complex is not pre-formed. For instance, as part of post-transcriptional silencing, AcrVIB1 could be applied to reduce leaky expression prior to Cas13 induction,[43,46,47] or it could restrict silencing to specific cell types through tissue-specific expression of the Acr.[48,49] Thus, further exploring the potential uses of Cas13 Acrs could expand and enhance current capabilities of CRISPR technologies.

### Limitations of the study

In this work, we provide multiple lines of evidence that AcrVIB1 inhibits CRISPR immunity by converting the PbuCas13b effector nuclease into a crRNA sink that more readily binds crRNA but blocks target-triggered collateral RNA cleavage while leaving the crRNA exposed to cellular RNases. However, there are some limitations that should be weighed when interpreting the presented results. First, the responsible RNases remain unknown and may vary between *E. coli* and the native host of the VI-B CRISPR-Cas system. We also cannot rule out the involvement of other host factors beyond RNases (e.g., chaperones and gene regulatory factors) that could contribute to the reduction in crRNA abundance *in vivo*. Second, we could not gain deeper structural insights due to the high flexibility of the AcrVIB1:PbuCas13b:crRNA complex as well as the lack of available target-bound structures, preventing us from elucidating the exact interactions between AcrVIB1 and other building blocks of PbuCas13b beyond the helical-2 domain. Further, a general understanding about how movements of the helical-2 domain are linked to crRNA processing, target RNA recognition and the activation of collateral RNA cleavage is still missing. Finally, our study was limited to PbuCas13b, the only nuclease tested to-date showing strong inhibition by AcrVIB1. It remains to be determined how this inhibitory mechanism extends to other inhibited Cas13b orthologs,[25] particularly if the weak crRNA binding associated with PbuCas13b we observed is both unique among Cas13 nucleases and impacts access of AcrVIB1 to the Cas13b holoenzyme.

## RESOURCE AVAILABILITY

### Lead contact

Further information and requests for resources and reagents should be directed to and will be fulfilled by the lead contact, Prof. Chase L. Beisel (chase.beisel@helmholtz-hiri.de).

### Materials availability

Key plasmids generated in this study have been deposited to Addgene. All other plasmids can be obtained upon reasonable request to Prof. Chase L. Beisel (chase.beisel@helmholtz-hiri.de).

### Data and code availability

- Original gel images for Figures 1, 2, 4, 5, 6, S2, S4, and S5 have been deposited in Mendeley Data (https://doi.org/10.17632/kvhr9y39pc.1). The Cas13b:crRNA structure (PBD: 9FCV) as well as the electron density maps of the Cas13b:crRNA complex (EMDB: EMD-50322), the Cas13b:crRNA:AcrVIB1 complex (EMDB: EMD-51509), and the AcrVIB1:PbuCas13b helical-2 domain complex (EMDB: EMD-51513) are available through the Protein Data Bank (https://www.rcsb.org/). Deposited data will be publicly available as of the date of publication.
- This paper does not report original code.
- Any additional information required to reanalyze the data reported in this paper is available from the lead contact upon request.

## ACKNOWLEDGMENTS

We express our gratitude to the protein expression facility of the Rudolf-Virchow-Zentrum (Center for Integrative and Translational Bioimaging) for their excellent support and expertise in protein purification. We would also like to thank Ute Widow for excellent technical assistance in protein production. Our appreciation also goes to Thomas Gaudin for assistance with experiments using the Echo 525 acoustic liquid handler and to Mitchell O'Connell for initial discussions and technical support. This work was supported by the Deutsche Forschungsgemeinschaft SPP 2141 program (BE 6703/1-2 to C.L.B.), a European Research Council Consolidator Award (865973 to C.L.B.), and internal funding from the Helmholtz Centre for Infection Research (to N.C., W.B., and C.L.B.).

## AUTHOR CONTRIBUTIONS

Conceptualization: K.G.W. and C.L.B.; experiments: K.G.W., S.S., A.M., A.K., P.L., and T.A.; writing – original draft: K.G.W., S.S., P.L., W.B., and C.L.B.; writing – review & editing: all authors; visualization: K.G.W., S.S., P.L., W.B., and C.L.B.; supervision: N.C., W.B., and C.L.B.; funding acquisition: N.C., W.B., and C.L.B.

## DECLARATION OF INTERESTS

C.L.B. is a co-founder and officer of Leopard Biosciences, co-founder and Scientific Advisor to Locus Biosciences, and Scientific Advisor to Benson Hill.

## STAR★METHODS

Detailed methods are provided in the online version of this paper and include the following:

- KEY RESOURCES TABLE
- EXPERIMENTAL MODEL AND STUDY PARTICIPANT DETAILS
- METHOD DETAILS
  - Buffers, plasmids, and oligos
  - Molecular cloning
  - Protein purification
  - RNA isolation
  - *In vitro* cleavage assays
  - Northern blotting analysis
  - Western blotting analysis
  - RNA labeling
  - Microscale thermophoresis and spectral shift
  - Co-immunoprecipitation
  - Complex generation, stability, and size analyses
  - Electrophoretic mobility shift assays
  - crRNA processing assay
  - RNA protection assays
  - Cryo-electron microscopy
  - SEC-MALS analysis
  - TXTL assays

Molecular Cell
Article

CellPress
OPEN ACCESS

## SUPPLEMENTAL INFORMATION

Supplemental information can be found online at https://doi.org/10.1016/j.molcel.2025.01.020.

Received: October 1, 2024
Revised: December 17, 2024
Accepted: January 21, 2025
Published: February 17, 2025

## REFERENCES

1. Rostøl, J.T., and Marraffini, L. (2019). (Ph)ighting Phages: How Bacteria Resist Their Parasites. Cell Host Microbe *25*, 184–194. https://doi.org/10.1016/j.chom.2019.01.009.
2. Payne, L.J., Todeschini, T.C., Wu, Y., Perry, B.J., Ronson, C.W., Fineran, P.C., Nobrega, F.L., and Jackson, S.A. (2021). Identification and classification of antiviral defence systems in bacteria and archaea with PADLOC reveals new system types. Nucleic Acids Res. *49*, 10868–10878. https://doi.org/10.1093/nar/gkab883.
3. Srikant, S., Guegler, C.K., and Laub, M.T. (2022). The evolution of a counter-defense mechanism in a virus constrains its host range. eLife *11*, e79549. https://doi.org/10.7554/eLife.79549.
4. Jackson, S.A., McKenzie, R.E., Fagerlund, R.D., Kieper, S.N., Fineran, P.C., and Brouns, S.J.J. (2017). CRISPR-Cas: Adapting to change. Science *356*, eaal5056. https://doi.org/10.1126/science.aal5056.
5. McGinn, J., and Marraffini, L.A. (2019). Molecular mechanisms of CRISPR-Cas spacer acquisition. Nat. Rev. Microbiol. *17*, 7–12. https://doi.org/10.1038/s41579-018-0071-7.
6. Makarova, K.S., Wolf, Y.I., Iranzo, J., Shmakov, S.A., Alkhnbashi, O.S., Brouns, S.J.J., Charpentier, E., Cheng, D., Haft, D.H., Horvath, P., et al. (2020). Evolutionary classification of CRISPR-Cas systems: a burst of class 2 and derived variants. Nat. Rev. Microbiol. *18*, 67–83. https://doi.org/10.1038/s41579-019-0299-x.
7. Altae-Tran, H., Kannan, S., Suberski, A.J., Mears, K.S., Demircioglu, F.E., Moeller, L., Kocalar, S., Oshiro, R., Makarova, K.S., Macrae, R.K., et al. (2023). Uncovering the functional diversity of rare CRISPR-Cas systems with deep terascale clustering. Science *382*, eadi1910. https://doi.org/10.1126/science.adi1910.
8. Li, Y., and Bondy-Denomy, J. (2021). Anti-CRISPRs go viral: The infection biology of CRISPR-Cas inhibitors. Cell Host Microbe *29*, 704–714. https://doi.org/10.1016/j.chom.2020.12.007.
9. Forsberg, K.J. (2023). Anti-CRISPR Discovery: Using Magnets to Find Needles in Haystacks. J. Mol. Biol. *435*, 167952. https://doi.org/10.1016/j.jmb.2023.167952.
10. Bondy-Denomy, J., Davidson, A.R., Doudna, J.A., Fineran, P.C., Maxwell, K.L., Moineau, S., Peng, X., Sontheimer, E.J., and Wiedenheft, B. (2018). A Unified Resource for Tracking Anti-CRISPR Names. CRISPR J. *1*, 304–305. https://doi.org/10.1089/crispr.2018.0043.
11. Yin, P., Zhang, Y., Yang, L., and Feng, Y. (2023). Non-canonical inhibition strategies and structural basis of anti-CRISPR proteins targeting type I CRISPR-Cas systems. J. Mol. Biol. *435*, 167996. https://doi.org/10.1016/j.jmb.2023.167996.
12. Hwang, S., and Maxwell, K.L. (2023). Diverse Mechanisms of CRISPR-Cas9 Inhibition by Type II Anti-CRISPR Proteins. J. Mol. Biol. *435*, 168041. https://doi.org/10.1016/j.jmb.2023.168041.
13. Marino, N.D. (2023). Phage Against the Machine: Discovery and Mechanism of Type V Anti-CRISPRs. J. Mol. Biol. *435*, 168054. https://doi.org/10.1016/j.jmb.2023.168054.
14. Bondy-Denomy, J., Garcia, B., Strum, S., Du, M., Rollins, M.F., Hidalgo-Reyes, Y., Wiedenheft, B., Maxwell, K.L., and Davidson, A.R. (2015). Multiple mechanisms for CRISPR-Cas inhibition by anti-CRISPR proteins. Nature *526*, 136–139. https://doi.org/10.1038/nature15254.
15. Chowdhury, S., Carter, J., Rollins, M.F., Golden, S.M., Jackson, R.N., Hoffmann, C., Nosaka, L., Bondy-Denomy, J., Maxwell, K.L., Davidson, A.R., et al. (2017). Structure Reveals Mechanisms of Viral Suppressors that Intercept a CRISPR RNA-Guided Surveillance Complex. Cell *169*, 47–57.e11. https://doi.org/10.1016/j.cell.2017.03.012.
16. Dong, D., Guo, M., Wang, S., Zhu, Y., Wang, S., Xiong, Z., Yang, J., Xu, Z., and Huang, Z. (2017). Structural basis of CRISPR–SpyCas9 inhibition by an anti-CRISPR protein. Nature *546*, 436–439. https://doi.org/10.1038/nature22377.
17. Meeske, A.J., Jia, N., Cassel, A.K., Kozlova, A., Liao, J., Wiedmann, M., Patel, D.J., and Marraffini, L.A. (2020). A phage-encoded anti-CRISPR enables complete evasion of type VI-A CRISPR-Cas immunity. Science *369*, 54–59. https://doi.org/10.1126/science.abb6151.
18. Lu, W.-T., Trost, C.N., Müller-Esparza, H., Randau, L., and Davidson, A.R. (2021). Anti-CRISPR AcrIF9 functions by inducing the CRISPR–Cas complex to bind DNA non-specifically. Nucleic Acids Res. *49*, 3381–3393. https://doi.org/10.1093/nar/gkab092.
19. Dong, L., Guan, X., Li, N., Zhang, F., Zhu, Y., Ren, K., Yu, L., Zhou, F., Han, Z., Gao, N., et al. (2019). An anti-CRISPR protein disables type V Cas12a by acetylation. Nat. Struct. Mol. Biol. *26*, 308–314. https://doi.org/10.1038/s41594-019-0206-1.
20. Sun, W., Cheng, Z., Wang, J., Yang, J., Li, X., Wang, J., Chen, M., Yang, X., Sheng, G., Lou, J., et al. (2023). AcrIIC4 inhibits type II-C Cas9 by preventing R-loop formation. Proc. Natl. Acad. Sci. USA *120*, e2303675120. https://doi.org/10.1073/pnas.2303675120.
21. Song, G., Zhang, F., Zhang, X., Gao, X., Zhu, X., Fan, D., and Tian, Y. (2019). AcrIIA5 Inhibits a Broad Range of Cas9 Orthologs by Preventing DNA Target Cleavage. Cell Rep. *29*, 2579–2589.e4. https://doi.org/10.1016/j.celrep.2019.10.078.
22. Thavalingam, A., Cheng, Z., Garcia, B., Huang, X., Shah, M., Sun, W., Wang, M., Harrington, L., Hwang, S., Hidalgo-Reyes, Y., et al. (2019). Inhibition of CRISPR-Cas9 ribonucleoprotein complex assembly by anti-CRISPR AcrIIC2. Nat. Commun. *10*, 2806. https://doi.org/10.1038/s41467-019-10577-3.
23. Wang, X., Li, X., Ma, Y., He, J., Liu, X., Yu, G., Yin, H., and Zhang, H. (2022). Inhibition mechanisms of CRISPR-Cas9 by AcrIIA17 and AcrIIA18. Nucleic Acids Res. *50*, 512–521. https://doi.org/10.1093/nar/gkab1197.
24. Marino, N.D., Talaie, A., Carion, H., Johnson, M.C., Zhang, Y., Silas, S., Li, Y., and Bondy-Denomy, J. (2022). Translation-dependent downregulation of Cas12a mRNA by an anti-CRISPR protein. Preprint at bioRxiv. https://doi.org/10.1101/2022.11.29.518452.
25. Wandera, K.G., Alkhnbashi, O.S., Bassett, H.V.I., Mitrofanov, A., Hauns, S., Migur, A., Backofen, R., and Beisel, C.L. (2022). Anti-CRISPR prediction using deep learning reveals an inhibitor of Cas13b nucleases. Mol. Cell *82*, 2714–2726.e4. https://doi.org/10.1016/j.molcel.2022.05.003.
26. Meeske, A.J., Nakandakari-Higa, S., and Marraffini, L.A. (2019). Cas13-induced cellular dormancy prevents the rise of CRISPR-resistant bacteriophage. Nature *570*, 241–245. https://doi.org/10.1038/s41586-019-1257-5.
27. Abudayyeh, O.O., Gootenberg, J.S., Konermann, S., Joung, J., Slaymaker, I.M., Cox, D.B.T., Shmakov, S., Makarova, K.S., Semenova, E., Minakhin, L., et al. (2016). C2c2 is a single-component programmable RNA-guided RNA-targeting CRISPR effector. Science *353*, aaf5573. https://doi.org/10.1126/science.aaf5573.
28. Wright, A.V., Sternberg, S.H., Taylor, D.W., Staahl, B.T., Bardales, J.A., Kornfeld, J.E., and Doudna, J.A. (2015). Rational design of a split-Cas9 enzyme complex. Proc. Natl. Acad. Sci. USA *112*, 2984–2989. https://doi.org/10.1073/pnas.1501698112.
29. East-Seletsky, A., O'Connell, M.R., Burstein, D., Knott, G.J., and Doudna, J.A. (2017). RNA Targeting by Functionally Orthogonal Type VI-A CRISPR-Cas Enzymes. Mol. Cell *66*, 373–383.e3. https://doi.org/10.1016/j.molcel.2017.04.008.

Please cite this article in press as: Wandera et al., AcrVIB1 inhibits CRISPR-Cas13b immunity by promoting unproductive crRNA binding accessible to RNase attack, Molecular Cell (2025), https://doi.org/10.1016/j.molcel.2025.01.020



30. Smargon, A.A., Cox, D.B.T., Pyzocha, N.K., Zheng, K., Slaymaker, I.M., Gootenberg, J.S., Abudayyeh, O.A., Essletzbichler, P., Shmakov, S., Makarova, K.S., et al. (2017). Cas13b Is a Type VI-B CRISPR-Associated RNA-Guided RNase Differentially Regulated by Accessory Proteins Csx27 and Csx28. Mol. Cell *65*, 618–630.e7. https://doi.org/10.1016/j.molcel.2016.12.023.

31. Slaymaker, I.M., Mesa, P., Kellner, M.J., Kannan, S., Brignole, E., Koob, J., Feliciano, P.R., Stella, S., Abudayyeh, O.O., Gootenberg, J.S., et al. (2019). High-Resolution Structure of Cas13b and Biochemical Characterization of RNA Targeting and Cleavage. Cell Rep. *26*, 3741–3751.e5. https://doi.org/10.1016/j.celrep.2019.02.094.

32. Abramson, J., Adler, J., Dunger, J., Evans, R., Green, T., Pritzel, A., Ronneberger, O., Willmore, L., Ballard, A.J., Bambrick, J., et al. (2024). Accurate structure prediction of biomolecular interactions with AlphaFold 3. Nature *630*, 493–500. https://doi.org/10.1038/s41586-024-07487-w.

33. Jumper, J., Evans, R., Pritzel, A., Green, T., Figurnov, M., Ronneberger, O., Tunyasuvunakool, K., Bates, R., Žídek, A., Potapenko, A., et al. (2021). Highly accurate protein structure prediction with AlphaFold. Nature *596*, 583–589. https://doi.org/10.1038/s41586-021-03819-2.

34. Zhang, B., Ye, W., Ye, Y., Zhou, H., Saeed, A.F.U.H., Chen, J., Lin, J., Perčulija, V., Chen, Q., Chen, C.-J., et al. (2018). Structural insights into Cas13b-guided CRISPR RNA maturation and recognition. Cell Res. *28*, 1198–1201. https://doi.org/10.1038/s41422-018-0109-4.

35. Camara-Wilpert, S., Mayo-Muñoz, D., Russel, J., Fagerlund, R.D., Madsen, J.S., Fineran, P.C., Sørensen, S.J., and Pinilla-Redondo, R. (2023). Bacteriophages suppress CRISPR-Cas immunity using RNA-based anti-CRISPRs. Nature *623*, 601–607. https://doi.org/10.1038/s41586-023-06612-5.

36. Knott, G.J., Thornton, B.W., Lobba, M.J., Liu, J.-J., Al-Shayeb, B., Watters, K.E., and Doudna, J.A. (2019). Broad-spectrum enzymatic inhibition of CRISPR-Cas12a. Nat. Struct. Mol. Biol. *26*, 315–321. https://doi.org/10.1038/s41594-019-0208-z.

37. Borges, A.L., Zhang, J.Y., Rollins, M.F., Osuna, B.A., Wiedenheft, B., and Bondy-Denomy, J. (2018). Bacteriophage Cooperation Suppresses CRISPR-Cas3 and Cas9 Immunity. Cell *174*, 917–925.e10. https://doi.org/10.1016/j.cell.2018.06.013.

38. Landsberger, M., Gandon, S., Meaden, S., Rollie, C., Chevallereau, A., Chabas, H., Buckling, A., Westra, E.R., and van Houte, S. (2018). Anti-CRISPR Phages Cooperate to Overcome CRISPR-Cas Immunity. Cell *174*, 908–916.e12. https://doi.org/10.1016/j.cell.2018.05.058.

39. Nicholson, T.J., Jackson, S.A., Croft, B.I., Staals, R.H.J., Fineran, P.C., and Brown, C.M. (2019). Bioinformatic evidence of widespread priming in type I and II CRISPR-Cas systems. RNA Biol. *16*, 566–576. https://doi.org/10.1080/15476286.2018.1509662.

40. Datsenko, K.A., Pougach, K., Tikhonov, A., Wanner, B.L., Severinov, K., and Semenova, E. (2012). Molecular memory of prior infections activates the CRISPR/Cas adaptive bacterial immunity system. Nat. Commun. *3*, 945. https://doi.org/10.1038/ncomms1937.

41. Powell, J.E., Lim, C.K.W., Krishnan, R., McCallister, T.X., Saporito-Magriña, C., Zeballos, M.A., McPheron, G.D., and Gaj, T. (2022). Targeted gene silencing in the nervous system with CRISPR-Cas13. Sci. Adv. *8*, eabk2485. https://doi.org/10.1126/sciadv.abk2485.

42. Kellner, M.J., Koob, J.G., Gootenberg, J.S., Abudayyeh, O.O., and Zhang, F. (2019). SHERLOCK: nucleic acid detection with CRISPR nucleases. Nat. Protoc. *14*, 2986–3012. https://doi.org/10.1038/s41596-019-0210-2.

43. Cox, D.B.T., Gootenberg, J.S., Abudayyeh, O.O., Franklin, B., Kellner, M.J., Joung, J., and Zhang, F. (2017). RNA editing with CRISPR-Cas13. Science *358*, 1019–1027.

44. Yang, L.-Z., Wang, Y., Li, S.-Q., Yao, R.-W., Luan, P.-F., Wu, H., Carmichael, G.G., and Chen, L.-L. (2019). Dynamic Imaging of RNA in Living Cells by CRISPR-Cas13 Systems. Mol. Cell *76*, 981–997.e7. https://doi.org/10.1016/j.molcel.2019.10.024.

45. Guan, J., Oromí-Bosch, A., Mendoza, S.D., Karambelkar, S., Berry, J.D., and Bondy-Denomy, J. (2022). Bacteriophage genome engineering with CRISPR-Cas13a. Nat. Microbiol. *7*, 1956–1966. https://doi.org/10.1038/s41564-022-01243-4.

46. Vialetto, E., Yu, Y., Collins, S.P., Wandera, K.G., Barquist, L., and Beisel, C.L. (2022). A target expression threshold dictates invader defense and prevents autoimmunity by CRISPR-Cas13. Cell Host Microbe *30*, 1151–1162.e6. https://doi.org/10.1016/j.chom.2022.05.013.

47. Abudayyeh, O.O., Gootenberg, J.S., Essletzbichler, P., Han, S., Joung, J., Belanto, J.J., Verdine, V., Cox, D.B.T., Kellner, M.J., Regev, A., et al. (2017). RNA targeting with CRISPR-Cas13. Nature *550*, 280–284.

48. Lee, J., Mou, H., Ibraheim, R., Liang, S.-Q., Liu, P., Xue, W., and Sontheimer, E.J. (2019). Tissue-restricted genome editing *in vivo* specified by microRNA-repressible anti-CRISPR proteins. RNA *25*, 1421–1431. https://doi.org/10.1261/rna.071704.119.

49. Hoffmann, M.D., Aschenbrenner, S., Grosse, S., Rapti, K., Domenger, C., Fakhiri, J., Mastel, M., Börner, K., Eils, R., Grimm, D., et al. (2019). Cell-specific CRISPR-Cas9 activation by microRNA-dependent expression of anti-CRISPR proteins. Nucleic Acids Res. *47*, e75. https://doi.org/10.1093/nar/gkz271.

50. Punjani, A., Rubinstein, J.L., Fleet, D.J., and Brubaker, M.A. (2017). cryoSPARC: algorithms for rapid unsupervised cryo-EM structure determination. Nat. Methods *14*, 290–296. https://doi.org/10.1038/nmeth.4169.

51. Rubinstein, J.L., and Brubaker, M.A. (2015). Alignment of cryo-EM movies of individual particles by optimization of image translations. J. Struct. Biol. *192*, 188–195. https://doi.org/10.1016/j.jsb.2015.08.007.

52. Punjani, A., Zhang, H., and Fleet, D.J. (2020). Non-uniform refinement: adaptive regularization improves single-particle cryo-EM reconstruction. Nat. Methods *17*, 1214–1221. https://doi.org/10.1038/s41592-020-00990-8.

53. Meng, E.C., Goddard, T.D., Pettersen, E.F., Couch, G.S., Pearson, Z.J., Morris, J.H., and Ferrin, T.E. (2023). UCSF ChimeraX: Tools for structure building and analysis. Protein Sci. *32*, e4792. https://doi.org/10.1002/pro.4792.

54. Pettersen, E.F., Goddard, T.D., Huang, C.C., Meng, E.C., Couch, G.S., Croll, T.I., Morris, J.H., and Ferrin, T.E. (2021). UCSF ChimeraX: Structure visualization for researchers, educators, and developers. Protein Sci. *30*, 70–82. https://doi.org/10.1002/pro.3943.

55. Poppenborg, L., Friehs, K., and Flaschel, E. (1997). The green fluorescent protein is a versatile reporter for bioprocess monitoring. J. Biotechnol. *58*, 79–88. https://doi.org/10.1016/s0168-1656(97)00134-x.

56. Studier, F.W. (2005). Protein production by auto-induction in high density shaking cultures. Protein Expr. Purif. *41*, 207–234. https://doi.org/10.1016/j.pep.2005.01.016.

57. Croll, T.I. (2018). ISOLDE: a physically realistic environment for model building into low-resolution electron-density maps. Acta Crystallogr. D Struct. Biol. *74*, 519–530. https://doi.org/10.1107/S2059798318002425.

58. Emsley, P., Lohkamp, B., Scott, W.G., and Cowtan, K. (2010). Features and development of Coot. Acta Crystallogr. D Biol. Crystallogr. *66*, 486–501. https://doi.org/10.1107/S0907444910007493.

59. Afonine, P.V., Poon, B.K., Read, R.J., Sobolev, O.V., Terwilliger, T.C., Urzhumtsev, A., and Adams, P.D. (2018). Real-space refinement in PHENIX for cryo-EM and crystallography. Acta Crystallogr. D Struct. Biol. *74*, 531–544. https://doi.org/10.1107/S2059798318006551.

60. Liebschner, D., Afonine, P.V., Baker, M.L., Bunkóczi, G., Chen, V.B., Croll, T.I., Hintze, B., Hung, L.W., Jain, S., McCoy, A.J., et al. (2019). Macromolecular structure determination using X-rays, neutrons and electrons: recent developments in Phenix. Acta Crystallogr. D Struct. Biol. *75*, 861–877. https://doi.org/10.1107/S2059798319011471.

Please cite this article in press as: Wandera et al., AcrVIB1 inhibits CRISPR-Cas13b immunity by promoting unproductive crRNA binding accessible to RNase attack, Molecular Cell (2025), https://doi.org/10.1016/j.molcel.2025.01.020



CellPress
OPEN ACCESS

## STAR★METHODS

### KEY RESOURCES TABLE

| REAGENT or RESOURCE | SOURCE | IDENTIFIER |
|---|---|---|
| **Antibodies** | | |
| IRDye® 680RD Goat anti-Rabbit IgG | LI-COR Biosciences - GmbH | Cat# 926-68071; RRID: AB_10956166 |
| IRDye® 800CW Goat anti-Mouse IgG | LI-COR Biosciences - GmbH | Cat# 926-32210; RRID: AB_621842 |
| 6x-His Tag Monoclonal Antibody (HIS.H8) | Life Technologies GmbH | Cat# MA121315; RRID: AB_557403 |
| ANTI-FLAG(R), ANTIBODY PRODUCED IN RABBIT | Sigma-Aldrich Chemie GmbH | Cat# F7425-.2MG; RRID: AB_439687 |
| Anti-His-Tag rabbit monoclonal antibody [RM146], Rabbit IgG, Unconjugated 100 | Biozol Diagnostica Vertrieb GmbH | Cat# RMB-31-1048-00-100; RRID: AB_2716427 |
| RABBIT ANTI-GRO-EL, IGG FRACTION | Sigma-Aldrich | Cat# G6532-.5ML; RRID: AB_259939 |
| **Bacterial and virus strains** | | |
| BL21(DE3) Competent *Escherichia coli* | New England Biolabs | C2527 |
| One Shot TOP10 Chemically Competent *Escherichia coli* | Thermo Fischer Scientific | C404010 |
| **Chemicals, peptides, and recombinant proteins** | | |
| Isopropyl-ß-D-thiogalactopyranosid (IPTG) | Carl Roth | Cat#2316.4; CAS: 367-93-1 |
| cOmplete™, Mini, EDTA-free Protease Inhibitor Cocktail | Roche | 11836170001 |
| TEV protease (pRK793), self-prepared | Addgene | pRK793, Plasmid #8827 |
| SUMO protease (SENP2), self-prepared | Addgene | pET28a-SENP2, Plasmid #16357 |
| NativeMark™ (MW standard for mass photometry) | Invitrogen/Thermo | LC0725 |
| **Critical commercial assays** | | |
| myTXTL Sigma 70 Master Mix Kit | Daicel Arbor Biosciences | 507025 |
| **Deposited data** | | |
| Images for Figures 1, 2, 4, 5, 6, S2, S4, and S5 | This paper; Mendeley Data | https://doi.org/10.17632/kvhr9y39pc.1 |
| Cas13b:crRNA structure | This paper | PDB: 9FCV |
| Cas13b:crRNA electron density map | This paper | EMDB: EMD-50322 |
| Cas13b:crRNA:AcrVIB1 electron density map | This paper | EMDB: EMD-51509 |
| AcrVIB1:PbuCas13b Helical-2 domain complex electron density map | This paper | EMDB: EMD-51513 |
| **Oligonucleotides** | | |
| For oligonucleotides, see Table S1 | This paper | N/A |
| **Recombinant DNA** | | |
| For plasmids, see Table S1 | This paper | N/A |
| **Software and algorithms** | | |
| cryoSPARC (version 4.5.3) | Punjani et al.[50]; Rubinstein and Brubaker[51]; Punjani et al.[52] | https://cryosparc.com/ |
| AlphaFold Server (AlphaFold 3) | Abramson et al.[32] | https://alphafoldserver.com/welcome |
| PyMOL 3.0.3 - Incentive Product | Schrodinger, LLC | https://www.pymol.org/ |
| ChimeraX 1.7.1 | Meng et al.[53]; Pettersen et al.[54] | https://www.cgl.ucsf.edu/chimerax/ |
| GraphPad Prism 10.3.0 | GraphPad Software | https://www.graphpad.com/features |
| MO.Control2 | Nanotemper | N/A |
| DiscoverMP (2.5.0) | Refeyn Ltd. | N/A |

(*Continued on next page*)

Please cite this article in press as: Wandera et al., AcrVIB1 inhibits CRISPR-Cas13b immunity by promoting unproductive crRNA binding accessible to RNase attack, Molecular Cell (2025), https://doi.org/10.1016/j.molcel.2025.01.020



*Continued*

| REAGENT or RESOURCE | SOURCE | IDENTIFIER |
|---|---|---|
| PR.Panta Analysis (1.7.1) | Nanotemper | N/A |
| Other | | |
| HisTrap HP 5 ml (IMAC column) | Cytiva | 17524801 |
| HiLoad 16/600 Superdex 200 pg (SEC column) | Cytiva | 28989335 |
| HiTrap Capto SP ImpRes 1 ml (CIX column) | Cytiva | 29400460 |
| HiTrap Heparin HP 5 ml (AIX column) | Cytiva | 17040703 |
| Superdex 75 10/300 GL (SEC column) | Cytiva | 29148721 |
| HiLoad 16/600 Superdex 75 pg (SEC column) | Cytiva | 17517401 |

## EXPERIMENTAL MODEL AND STUDY PARTICIPANT DETAILS

Two strains of *Escherichia coli* were used in this work: BL21(DE3) Competent *E. coli* and One Shot TOP10 Chemically Competent *E. coli*. Both strains were cultured in LB medium with shaking at 37°C and 220 rpm unless indicated otherwise in the methods. Both strains are stored as glycerol stocks at -80°C.

## METHOD DETAILS

### Buffers, plasmids, and oligos

All resources are listed in Table S1.

### Molecular cloning

All plasmids were cloned using standard cloning techniques: Q5 mutagenesis, Gibson Assembly and Golden Gate Cloning. Cloned sequences were verified by Sanger sequencing or Nanopore sequencing. Descriptions and links for each plasmid can be found in Table S1.

### Protein purification

The gene encoding AcrVIB1 from *Riemerella anatipestifer* (WP_004917816.1) was overexpressed and purified from t was cloned into a modified pCOLA Duet-1 vector (Novagen) encoding for an N-terminal Hisactophilin tag[55] and TEV-protease recognition site (KW-426). The gene encoding for PbuCas13b was cloned into pETM11 together with N-terminal hexahistidine and SUMO tags (KW-241). A construct for the Helical-2 domain of PbuCas13b was designed comprising the residues 579 - 747 and the mutations Q580C and T745C in order to form an artificial disulfide bridge for stabilization of the isolated domain. The construct was sourced commercially as a synthetic gene (GenScript) together with a Strep-tag II, a Hisactophilin tag[55] and a TEV-protease recognition site at the N terminus and cloned into pET28a (PL-001).

All proteins were expressed in *E. coli* BL21 (DE3) Star in baffled shaking flasks with 1 L of ZYM-5052 auto-inducing medium[56] each at 20°C for 20-24 h.

For the purification of AcrVIB1, the cell pellet was resuspended in a buffer containing 20 mM HEPES/NaOH pH 7.5, 300 mM NaCl, 1 mM TCEP, 20 mM imidazole and one tablet of cOmplete EDTA-free protease inhibitor cocktail (Roche). After lysis by sonication, the protein was isolated from the supernatant after centrifugation for 1 h at 100,000 x g using a 5 ml HisTrap HP column (Cytiva) and eluted using a linear gradient towards 500 mM imidazole. The affinity tag was cleaved off with TEV protease (1:50 mg/mg) at 4°C during overnight dialysis against imidazole-free buffer. Gel filtration was carried out using a HiLoad 16/600 Superdex 200 pg column (Cytiva) in 20 mM HEPES/NaOH pH 7.5, 300 mM NaCl, 1 mM TCEP. The peak fractions were concentrated, flash-frozen in liquid nitrogen and stored at -80°C.

For the preparation of PbuCas13 for cryo-EM analysis, the cell pellet was resuspended in a buffer containing 50 mM HEPES/NaOH pH 7.5, 500 mM NaCl, 0.5 mM DTT and 20 mM imidazole, plus one tablet of cOmplete EDTA-free protease inhibitor cocktail (Roche). After lysis by sonication, the protein was isolated from the supernatant after centrifugation for 1 h at 100,000 x g using a 5-ml HisTrap HP column (Cytiva) and eluted using a linear gradient towards 250 mM imidazole. The affinity and SUMO tags were cleaved off with SENP2 (1:50 mg/mg) at 4°C during overnight dialysis against SEC buffer (20 mM HEPES/NaOH pH 7.5, 300 mM NaCl, 0.5 mM DTT). Gel filtration was carried out using a HiLoad 16/600 Superdex 200 pg column (Cytiva) in 20 mM HEPES/NaOH pH 7.5, 300 mM NaCl, 1 mM TCEP. The peak fractions were concentrated and subjected to cation exchange chromatography using a 1-mL HiTrap Capto SP ImpRes column (Cytiva) with a buffer containing 20 mM HEPES/NaOH pH 7.0, 400 mM NaCl and 2 mM DTT. The protein was

Please cite this article in press as: Wandera et al., AcrVIB1 inhibits CRISPR-Cas13b immunity by promoting unproductive crRNA binding accessible to RNase attack, Molecular Cell (2025), https://doi.org/10.1016/j.molcel.2025.01.020



eluted using a linear gradient from 400 mM NaCl to 1 mM NaCl. Peak fractions were pooled, resulting in a final NaCl concentration of 620 mM in the buffer. The samples were flash-frozen in liquid $N_2$ for cryo-EM analysis. For cryo-EM analysis, PbuCas13 samples were diluted to 1 mg/ml in 20 mM HEPES/NAOH pH 7.0, 120 mM NaCl prior complex formation.

For biophysical analyses of PbuCas13b, cell pellets were resuspended in lysis buffer (20 mM HEPES/NaOH pH 7.5, 500 mM NaCl, 10 mM $Na_3$-citrate, 10 mM $MgSO_4$ and 5 mM DTT) prior to sonication. Affinity purification was conducted using several steps of lysis buffer with increasing imidazole concentrations. The desired protein eluted between 62.5 and 100 mM imidazole. Fractions of 2.5 ml were collected into tubes pre-filled with 5 ml of imidazole-free buffer. After cleavage with SENP2, anion exchange was performed using a 5 ml HiTrap Heparin column (Cytiva) in lysis buffer with a linear gradient from 0.5 M – 2 M NaCl. The elution peak was concentrated and subjected to gel filtration using a HiLoad 16/600 Superdex 200 pg column (Cytiva) in 20 mM HEPES/NaOH pH 7.5, 300 mM NaCl and 5 mM DTT. Peak fractions were concentrated and flash-frozen in liquid nitrogen.

For the purification of the PbuCas13b Helical-2 domain, the cell pellet was resuspended in a buffer containing 20 mM HEPES/NaOH pH 7.5, 150 mM NaCl, 20 mM imidazole and one tablet of cOmplete EDTA-free protease inhibitor cocktail (Roche). After lysis by sonication, the protein was isolated from the supernatant after centrifugation for 1 h at 37,000 x g using a 5 ml HisTrap HP column (Cytiva) and eluted using steps of increasing imidazole concentrations. The protein eluted at a concentration of 500 mM imidazole. The affinity tag was cleaved off with TEV protease (1:50 mg/mg) at 4°C. Gel filtration was carried out using a HiLoad 16/600 Superdex 75 pg column (Cytiva) in 20 mM HEPES/NaOH pH 7.5, 150 mM NaCl. The peak fractions were concentrated, flash-frozen in liquid nitrogen and stored at -80°C.

All chromatography steps were executed using an Äkta Go chromatography system (Cytiva).

### RNA isolation

Total RNA was isolated using a phenol-chloroform extraction method. Bacterial cultures were cultivated until reaching a maximum optical density (OD) of 1 and subsequently harvested to obtain an overall OD of 4. This was achieved, for instance, by collecting 4 mL of culture with an optical density of 1. A mixture of 95% EtOH (Sigma-Aldrich, 32221-M) and 5% phenol (Carl Roth, #A980.1) was added to each culture in a volume ratio of 1:5 from the initial culture volume, which was then immediately transferred to liquid nitrogen. Samples were placed on ice until all samples were thawed (45-60 min). Cells were pelleted at 7,400 rpm for 20 min at 4°C. Supernatant was carefully removed before centrifuging all samples again at 7,400 rpm for 1 min at 4°C. All remaining supernatant was removed. All samples were resuspended using 600 μL of 0.5 mg/ml lysozyme (Carl Roth, #8259.2) solved in TE buffer pH 8.0. After transferring all samples to a 2 mL tube, 60 μL of 10% w/v SDS was added and mixed by inversion. Tubes were placed in a water bath at 64°C for 1-2 min (the samples should become clear). To each sample, 66 μL of 3 M NaOAc, pH 5.2 was added and mixed by inversion. Equal volumes (750 μL) of phenol (Carl Roth, #A980.1) were added to the samples, and the samples were incubated for 6 min at 64°C. Samples were inverted every 30 s during the incubation process. Subsequently, all tubes were chilled on ice, before they were centrifuged at full speed (13,000 rpm) for 15 min at 12°C. The aqueous layer was transferred into 5PRIME Phase Lock Gel (PLG) tubes (VWR International, #733-2478). An equal volume (750 μL) of chloroform (Roth, #Y015.2) was added in each PLG tube and mixed by inversion. All samples were spun down at full speed for 15 min at 12°C. After that, the aqueous layer was transferred into 2 mL of RNAse-free tubes. To each sample, 2.5 volumes of a 30:1 mix of EtOH:NaAcetate (3 M, pH 6.5) was added. Samples were incubated at -80°C for at least 20 min up to 2 h. Subsequently, all samples were spun down at 15,000 g for 30 min at 4°C. The extracted RNA was washed with 500 μL of 70% EtOH and spun for 10 min at 15,000 g at 4°C. The wash step is repeated using 100% EtOH. All EtOH was aspirated and the RNA samples were dried at room temperature for 20 min before resuspending the RNA in 50 to 100 μL of RNase-free water. The concentration of each extracted RNA was determined using a Nanodrop.

### *In vitro* cleavage assays

Collateral RNA degradation is measured using a fluorescence-based assay, where a labeled RNA FAM reporter is added together with purified PbuCas13b, a corresponding crRNA and the matching target RNA. Different combinations of components were added together and incubated at room temperature for 15 min. All remaining components were subsequently added. The FAM reporter was always added last. All shown data was produced using the Echo525 Liquid Handling system. A plate reader was used to measure fluorescence over time. Raw data was imported into R (R version 4.2.0 (2022-04-22)) from.csv files using the readxl package (version readxl_1.4.3). Data wrangling was performed via the R packages dplyr (version dplyr_1.1.4), tidyr (version tidyr_1.3.0), and stringr (version stringr_1.5.1). Data of multiple experiments was merged and fluorescence intensities for each experiment were scaled to values between zero and one (minmax). Endpoints were selected manually to show data below maximum fluorescence intensity. Data visualizations were created using ggplot2 (version ggplot2_3.4.4). Calculation of the remaining collateral activity of PbuCas13b was calculated using the following formula:

$$Collateral\ activity\ (\%) = \left(1 - \frac{Mean_{Fluorescence-Acr} - Mean_{Fluorescence+Acr}}{Mean_{Fluorescence-Acr}}\right) x\ 100$$

The standard deviation was calculated using the following formula:

$$Standard\ deviation = \sqrt{\sigma^2_{(-Acr)} + \sigma^2_{(+Acr)}}$$

Please cite this article in press as: Wandera et al., AcrVIB1 inhibits CRISPR-Cas13b immunity by promoting unproductive crRNA binding accessible to RNase attack, Molecular Cell (2025), https://doi.org/10.1016/j.molcel.2025.01.020



To observe target RNA degradation, 0.2 μM PbuCas13b and 1 or 5 μM AcrVIB1 were pre-incubated for 15 min at room temperature in nuclease buffer (10 mM TrisHCl pH 7.5, 50 mM NaCl, 0.5 mM MgCl2, 0.1% BSA), then 100 nM of crRNA (KW-RNA-002) was added. The reaction was incubated for another 15 min at room temperature, followed by addition of 10 nM Cy5-3′-labeled and 600 nM of unlabeled target RNA (KW-RNA-005). The reaction was incubated at room temperature for 1 h. An equal volume of 2X RNA-loading dye (10 M Urea, 0.5 mM EDTA) was added, samples were denatured at 95°C for 2 min and separated on a 10% PAAG-7M urea-TBE. The gels were visualized using an Amersham Typhoon imaging system. The assays were performed in two replicates.

### Northern blotting analysis

For northern blotting analysis, 10 μg of each total RNA sample were mixed with 2x GLII loading buffer (NEB, Cat. no. B0363A), boiled at 95°C for 5 min in a closed vial and loaded on an 8% polyacrylamide gel containing 7 M urea for electrophoresis-based molecules separation at 300 V for 140 min using a gel transfer system (Doppel-Gelsystem Twin L, PerfectBlue-VWR).

After electrophoresis, RNA was transferred to Hybond-XL membranes (BLOTTING-NYLON 66 MEMBRANES,TYPE B, POS. 15356-1EA, Sigma-Aldrich) using an electroblotter with an applied voltage of 50 V for 1 h at 4°C (tank electroblotter Web M, PerfectBlue), cross-linked with UV light at 0.12 joules (UV lamp T8C; 254 nm, 8W), hybridized overnight in 15 mL of Roti Hybri-Quick buffer (A981.1, Carl Roth) at 42°C with 5 μL of $\gamma$ $^{32}$P-ATP end-labeled oligodeoxyribonucleotides and visualized after one day of exposure on a phosphorimager (Typhoon FLA 7000, GE Healthcare). Oligonucleotides KW-pr-610 and KW-pr-725 were used to generate the blot analysis in Figure 2C. Loading uniformity was confirmed with the control-oligonucleotide binding to the ribosomal 5S RNA.

### Western blotting analysis

Samples for western blot were prepared by adding 1X Loading Dye and boiling them at 95°C for 10 min. Samples were loaded together with PageRuler Plus Prestained Protein Ladder (LIFE Technologies, #26619) in a 4-20% Mini-PROTEAN TGX Precast Protein Gel (Bio-Rad Laboratories, #4561095). The gels were placed in a clean plastic electrophoresis chamber and corresponding gel holder together with 1X SDS Running Buffer, the electrophoresis machine was connected to a power supply and all gels were run at 20 mA (60 V) for 20 min and then at 40 mA (120 V) for 45 min. Afterward, the gels were transferred to a Trans-Blot Turbo Mini 0.2 μm PVDF Transfer Pack (Bio-Rad Laboratories, #1704156) and blotted for 7 min using the Trans-Blot Turbo Transfer System. The blots were incubated in 5% nonfat dry milk prepared in 1X Tris-buffered saline with Tween 20 (TBS-T, VWR International, #J63682.K2) for 30 min at room temperature to block nonspecific binding sites. Primary antibodies were diluted in 5% nonfat dry milk according to the manufacturer's protocol and added to the appropriate blots overnight at 4°C. All blots were washed three times for 20 min using 1X TBS-T before adding the appropriate secondary antibody. Blots were then incubated at room temperature for 1 h. Subsequently, blots were washed again three times for 5 min each using 1X TBS-T. The Odyssey CLx LI-COR was used for imaging.

### RNA labeling

For the 5′-end labeling of RNA with Cy5 used for EMSA, MST, RNA protection assay, synthetic oligoribonucleotides (IDT) were labeled with Cy5 maleimide conjugates (#GEPA15131, Sigma-Aldrich) using the 5′ EndTag kit (#VEC-MB-9001, BIOZOL) as directed by the manufacturer.

For the 3′-end labeling of RNA with Cy5 used for EMSA, crRNA processing assay, synthetic oligoribonucleotides (IDT) were treated with T4 RNA ligase (#EL0021, Thermo Fisher Scientific) in the presence of pCp-Cy5 (#NU-1706-CY5, Jena Bioscience). The labeled RNA was purified with RNA Clean and Concentrator columns-5 (#R1013, Zymo Research).

### Microscale thermophoresis and spectral shift

For the labeled AcrVIB1 binding experiments, AcrVIB1-His was labeled using the Monolith His-Tag Labeling Kit RED-tris-NTA 2nd Generation kit (Nanotemper, MO-L018) according to the manufacturer's instructions. For each binding experiment, AcrVIB1 was diluted to 20 nM using a binding buffer used previously for EMSA experiments. A series of 16 tubes with PbuCas13b or crRNA dilutions were prepared using the binding buffer, producing ligand concentrations ranging from 120 pM to 4 μM for PbuCas13b and 3 nM to 100 μM for crRNA. For measurements, each ligand dilution was mixed with one volume of labeled AcrVIB1, which led to a final concentration of 10 nM of labeled AcrVIB1 and 60 pM to 2 μM of Cas13b and 1.5 nM to 50 μM of crRNA. For the labeled RNA-binding experiments, labeled crRNA was diluted to 10 nM in the binding buffer. To form the RNP complex, 2 nM of Pbucas13b and 10 nM of labeled crRNA were pre-incubated for 15 min at room temperature in the binding buffer. To form the AcrVIB1:PbuCas13b complex, 105 μM of AcrVIB1 and 21 μM of PbuCas13b were pre-incubated for 15 min at room temperature in the binding buffer. A series of 16 tubes with PbuCas13b, AcrVIB1 or (AcrVIB1+PbuCas13b) complex dilutions were prepared in binding buffer, producing ligand concentrations ranging from 640 pM to 21 μM for PbuCas13b, 600 pM to 20 μM for AcrVIB1 and 300 pM to 10.5 μM for the complex. For the measurement, each PbuCas13b and complex ligand dilutions were mixed with one volume of labeled crRNA. Similarly, each AcrVIB1 dilution was mixed with one volume of the labeled RNP complex, which led to a final crRNA concentration of 5.0 nM in all reactions. When monitoring the RNA target binding, first the RNP complex was formed with 3 μM of unlabeled crRNA and 6 μM of PbuCas13b. The RNP was serially diluted and then 10 nM Cy5-5'-end-labeled target was added to each dilution yielding final concentrations of 22 pM - 1.5 μM of the RNP complex and 5 nM of labeled target RNA. Similar experiments were conducted to observe the effect of AcrVIB1 on target binding. Here, 6 μM PbuCas13b and 30 μM AcrVIB1 were pre-incubated

Please cite this article in press as: Wandera et al., AcrVIB1 inhibits CRISPR-Cas13b immunity by promoting unproductive crRNA binding accessible to RNase attack, Molecular Cell (2025), https://doi.org/10.1016/j.molcel.2025.01.020



CellPress
OPEN ACCESS

for 15 min at room temperature in the binding buffer, followed by incubation with 3 μM of unlabeled crRNA for 15 min at room temperature.

Following the addition of the labeled targets to the ligand dilutions, the reactions were mixed by pipetting, incubated for 15 min at room temperature. In case of target RNA-binding, reactions were incubated for 15 min at 37°C. Capillary forces were used to load the samples into Monolith NT.115 Premium Capillaries (NanoTemper Technologies). Measurements were performed using a Monolith Pico instrument (NanoTemper Technologies) at an ambient temperature of 25°C. Instrument parameters were adjusted to 5% LED power, medium MST power, and MST on-time of 1.5 s. An initial fluorescence scan was performed across the capillaries to determine the sample quality and afterward, 16 subsequent thermophoresis measurements were performed. Data of three independently pipetted measurements were analyzed for the $\Delta F_{norm}$ values determined by the MO.Affinity Analysis software (NanoTemper Technologies). Graphs were plotted and binding affinities (linear regression model – one site specific model) were calculated using GraphPad Prism 9.2.0.

Binding affinities for AcrVIB1 titrated with the Helical-2 domain of PbuCas13b were obtained using a MonolithX instrument (NanoTemper Technologies) using both Spectral Shift and MST mode for evaluation. AcrVIB1 was fluorescently labeled using a Cy5-NHS ester by mixing 100 μL of a 20 μM protein solution with 100 μL of 60 μM dye. The reaction was carried out at room temperature for 30 minutes in 20 mM HEPES/NaOH pH 7.5, 150 mM NaCl. Excess dye was removed using a desalting column. The degree of labeling of AcrVIB1 with Cy5 was 30.8%. A dilution series of the non-labeled PbuCas13b Helical-2 domain was mixed with a constant concentration of Cy5-labeled AcrVIB1, resulting in 16 samples with 100 nM AcrVIB1 each and 50 μM Helical-2 domain as the highest ligand concentration in 20 mM HEPES/NaOH pH 7.5, 150 mM NaCl, 0.05% (v/v) Tween20. Affinity measurements were carried out in Premium Capillaries (NanoTemper Technologies) with 20% excitation power at 25°C. Binding was evaluated using both modes of the MonolithX device. In Spectral Shift mode, the 670 nm / 650 nm emission ratio of the initial fluorescence scans was evaluated to detect a bathochromic or hypsochromic shift of the dye induced by ligand binding. In MST mode, fluorescence was monitored at 670 nm and evaluated at 1.5 s on-time of the IR-laser at medium power. Data of four independent replicates were exported from the MO.Control2 software (NanoTemper Technologies) with conversion to $\Delta F_{norm}$ values for evaluation in MST mode. Graphs were plotted and binding affinities (nonlinear regression model – [Agonist] vs. response (three parameters)) were calculated using GraphPad Prism 10.3.0.

### Co-immunoprecipitation

To observe interactions between PbuCas13b-FLAG and AcrVIB1-His, Co-IP experiments were performed. For this, the purified labeled proteins were added together in 1x PBS at room temperature before adding them to Dynabeads Protein A labeled with either FLAG- or His-antibodies according to the manufacturer's recommendations (LIFE Technologies, #10006D). First, the antibody for the target protein was incubated with the Dynabeads Protein A in a tube for 10 min. Excess antibody was washed away by placing the tube in a magnetic rack and removing the supernatant. To immunoprecipitate the target antigen, samples were mixed with the magnetic beads and rotated for 10 min at RT to allow the antigen to bind to the magnetic bead-Ab complex. The magnetic bead-Ab-Ag complex was washed three times using 200 μL of Washing Buffer for each wash step. After washing, the magnetic bead-Ab-Ag complex was resuspended in 100 μL of Washing Buffer and the bead suspension was transferred to a clean tube to avoid coelution of proteins bound to the tube wall. To elute the target antigen, 20 μL of Elution Buffer and 20 μL of 1X Protein Loading Buffer were added to the magnetic bead-Ab-Ag mix. After gently pipetting to resuspend the magnetic bead-Ab-Ag complex, the samples were boiled for 5 min at 95°C. The samples were subsequently used for western blotting analysis.

### Complex generation, stability, and size analyses

Complexes of full-length PbuCas13b were formed in 100-μl samples by incubation of the protein (5 μM) with 1.5-fold molar excess of ligands. For complexes containing either unprocessed cRNA (KW-RNA-001) or AcrVIB1, the samples were incubated for 1 h at room temperature after addition of the corresponding ligand. For complexes with three components, a second ligand (either AcrVIB1 or cRNA) was added for overnight incubation at 4°C. Samples were after incubation centrifuged for 10 min at maximum speed in a benchtop microcentrifuge.

The complex of AcrVIB1 and the Helical-2 domain of PbuCas13b was formed by mixing equimolar amounts of both proteins and subjecting the mixture directly onto a Superdex 75 gel filtration column of appropriate volume equilibrated in 20 mM HEPES/NaOH pH 7.5, 150 mM NaCl.

Stability analyses were performed in a Prometheus Panta instrument (Nanotemper). Samples were in triplicates heated up to 95°C from 25°C at 3°C/min. Unfolding/Aggregation was followed by observing changes in the intrinsic fluorescence of aromatic residues up on unfolding of the proteins (350/330 nm fluorescence ratio), turbidity measured by static light scattering and the increase in cumulant hydrodynamic radius by dynamic light scattering.

Sizes of the full-length PbuCas13b complexes were determined by mass photometry in a TwoMP instrument (Refeyn Ltd). The samples were diluted to 100 nM and 1 μL of sample was added to 9 μL of buffer on the glass slide of the mass photometer. Movies of 90-s length were recorded for each sample at normal field of view in AcquireMP (Refeyn Ltd). Evaluation was performed in DiscoverMP (Refeyn Ltd) on the last 1500 counts recorded in each movie. Molecular masses were determined by matching histogram contrast against a molecular weight standard (Invitrogen/Thermo NativeMark™, LC0725).

Please cite this article in press as: Wandera et al., AcrVIB1 inhibits CRISPR-Cas13b immunity by promoting unproductive crRNA binding accessible to RNase attack, Molecular Cell (2025), https://doi.org/10.1016/j.molcel.2025.01.020



### Electrophoretic mobility shift assays

For the electrophoretic mobility shift assays (EMSAs), first 0.2 μM PbuCas13b and 0.1 or 1 μM AcrVIB1 were pre-incubated for 15 min at room temperature in a binding buffer (10 mM TrisHCl pH 7.5, 50 mM NaCl, 0.1% BSA, 10 mM EDTA, 5% glycerol) in the presence of 1 μg/μL of yeast RNA (#AM2283, Ambion) to enhance specific RNA-protein interaction, then 5 nM of the Cy5-5′-labeled crRNA (KW-RNA-002) was added. The reaction was incubated for another 15 min at room temperature.

When monitoring the target RNA binding, first 100 nM unlabeled crRNA (KW-RNA-002) was incubated for 15 min at room temperature with the pre-incubated proteins, then 5 nM Cy5-3′-labeled target (KW-RNA-005) was added. The reaction was incubated for another 15 min at 37°C.

The samples were separated on a 2% agarose-TBE gel at 4°C. The gels were visualized using an Amersham Typhoon imaging system. The assays were performed in two replicates.

### crRNA processing assay

For the in vitro processing assay, 0.2 μM of PbuCas13b and 0.1 or 1 μM of AcrVIB1 were pre-incubated for 15 min at room temperature in a nuclease buffer (10 mM TrisHCl pH 7.5, 50 mM NaCl, 0.5 mM $MgCl_2$, 0.1% BSA), then 5 nM Cy5-3′end-labeled extended crRNA (KW-RNA-001) was added. The reaction was incubated for another 15 min at 37°C. All reactions were prepared in 10 μL and were stopped by adding 10 μL of colorless gel-loading solution (10 M urea, 1.5 mM EDTA, pH 8.0) on ice. The samples were separated on 10% PAAG-7M urea. The gels were visualized using an Amersham Typhoon imaging system. The assays were performed in two replicates.

### RNA protection assays

For the RNA protection assay, 1 μM of PbuCas13b and 5 (RNase T1) or 50 (RNase A) μM of AcrVIB1 were pre-incubated for 15 min at room temperature in a cleavage buffer (10 mM HEPES pH 7.0, 250 mM NaCl, 5 mM $MgCl_2$, 1 mM DTT, 0.05% Tween 20) in the presence of 1 μg/μL of yeast RNA (#AM2283, Ambion), then 5 nM of the Cy5-5′-labeled crRNA (KW-RNA-002) was added. After the reaction was incubated for another 15 min at room temperature, it was treated with the 1 U/μL of RNase T1 (#AM2283, Ambion) or 0.1 ng/μL of RNase A (#EN0531, Thermo Scientific™) for 30 min at 37°C. All reactions were prepared in a total volume of 10 μL and were stopped by adding 10 μL of colorless gel-loading solution (10 M urea, 1.5 mM EDTA, pH 8.0) on ice. Shortly before loading, the samples were heat denatured at 94°C for 2 min and then were separated on a 6 (RNase T1) or 10% (RNase A) PAA-7M urea gel. The gels were visualized using an Amersham Typhoon imaging system. The assays were performed in two replicates. The data was analyzed with GraphPad Prism 9.3.0.

### Cryo-electron microscopy

#### *Cryo-EM grid preparation*

For the PbuCas13b:crRNA complex 1 mg/ml, for the PbuCas13b:AcrVIB1:crRNA complex 0.25 - 0.5 mg/ml and for the AcrVIB1:PbuCas13b Helical-2 domain complex 0.165 mg/ml SEC-purified samples were used for vitrification. 3.5-μL aliquots of each sample were applied to holey carbon grids (Quantifoil Cu R1.2/1.3, 200 mesh) that were glow discharged for 100 s at a current of 15 mA using a PELCO easiGlow™ glow discharger (Ted Pella, Inc). The grids were then blotted once with filter paper for 4.5 sec to remove excess liquid and plunge-frozen in liquid ethane using a FEI Vitrobot Mark IV (Thermo Fisher Scientific Ltd) at 4 - 10°C and 100% humidity.

#### *Cryo-EM data acquisition*

All cryo-EM data presented here were collected on a Glacios TEM equipped with a Selectris energy filter, and data collection parameters are detailed in Table 1. The microscope was operated in EFTEM mode with a slit-width of 10 eV and using a 70 μm objective aperture. Automated data acquisition was performed using EPU (Thermo Fisher Scientific). For the PbuCas13b:crRNA complex, 3,778 movies were collected, and for the PbuCas13b:AcrVIB1:crRNA complex, several datasets totaling 10,707 movies were collected. 8206 movies were collected for the AcrVIB1:PbuCas13b Helical-2 domain complex.

#### *Image processing*

Cryo-EM data analysis was conducted using cryoSPARC (version 4.5.3).[50–52] For the PbuCas13b:crRNA complex, standard procedures including CTF correction, motion correction, and particle picking were employed. Over 3.3 million particles were picked by the template picker and initially classified by a hetero refinement. The best class, comprising around 1.9 million particles, underwent further 2D classification to remove debris and broken particles. From the remaining 1 million particles, iterative particle cleaning was achieved through multiple rounds of heterogeneous refinement and 2D classifications. For the final set of 356,629 cleaned particles, reference-based motion correction was performed followed by non-uniform refinement in cryoSPARC. The final reconstruction achieved an overall resolution of 3.09 Å, determined by Fourier shell correlation at a 0.143 cut-off.

For the PbuCas13b:AcrVIB1:crRNA datasets, the same processing route was followed. In template-based particle picking, over 5.4 million particles were extracted. These underwent classification in a heterogeneous refinement, with the largest class containing 1.25 million particles. Subsequent 2D classification revealed a mixture of closed and open particle views. The subclass of the open form of PbuCas13b:AcrVIB1:crRNA was separated from the closed form through several rounds of 2D classifications and a final 3D classification. The remaining 302,661 particles were further classified by heterogeneous refinements and 3D classifications into three final subclasses of the open form of PbuCas13b:AcrVIB1:crRNA. The particle numbers for the final subclasses ranged from 74,499 to

Please cite this article in press as: Wandera et al., AcrVIB1 inhibits CRISPR-Cas13b immunity by promoting unproductive crRNA binding accessible to RNase attack, Molecular Cell (2025), https://doi.org/10.1016/j.molcel.2025.01.020



CellPress
OPEN ACCESS

120,153 particles per class. The final reconstructions of each subclass had an overall resolution ranging from 4.23 Å to 4.49 Å, determined by Fourier shell correlation at a 0.143 cut-off.

The initial AcrVIB1:PbuCas13b Helical-2 domain complex dataset comprised approx. 7.2 Mio particles. With a subset of this data, six ab-initio models were created and used to classify the 7.2 Mio particles by a heterogeneous refinement followed by a non-uniform refinement. The best model/particles were subjected to several iterative 2D classifications and non-uniform refinements to result in a 1,078,020 large particle set that refined to 5.11 Å as determined by Fourier shell correlation at a 0.143 cut-off. Cryo-EM data and refinement statistics are summarized in Table 1.

### *Structure refinement and model building*

The crystal structure model of a PbuCas13b:crRNA complex (PDB: 6DTD) served as initial template and was rigid-body fitted into the cryo-EM density within UCSF ChimeraX[53,54] using Isolde[57] and manually adjusted and rebuilt in Coot.[58] Several rounds of real-space refinement were performed in the PHENIX software suite[59,60] before final validation. The final structure was refined and validated before being deposited into the protein database with the PDB code 9FCV. The final electron density map was deposited at EMDB with the accession code EMD-50322.

For the various flexible open forms of the PbuCas13b:AcrVIB1:crRNA complex, the final model of the PbuCas13b:crRNA complex was superposed onto the resulting maps of the three subclasses. The flexible arm region and the RNA 5′ end were manually adjusted and fitted with Isolde due to low and poor density in this region. No real-space refinement was performed, and no final model of the corresponding subclasses was deposited, but the final electron density map was deposited and has the accession code EMD-51509.

The AlphaFold3 derived model of the AcrVIB1:PbuCas13b Helical-2 domain complex was superposed into the map of the AcrVIB1:PbuCas13b Helical-2 domain complex using UCSF ChimeraX "fit in map" base tool functionality without further model modifications applied. The final map was deposited and has the accession code EMD-51513.

### SEC-MALS analysis

For analysis of the total mass of AcrVIB1 in complex with the Helical-2 domain of PbuCas13b we applied analytical size exclusion chromatography in combination with multi angle light scattering (SEC-MALS). Therefore, we applied 135 ug protein to a Superdex 75 Increase 10/300 GL column (Cytiva) coupled to our MALS-System, comprising an Agilent 1260 Infinity II HPLC system (Santa Clara, USA), a mini-DAWN TREOS II multi-angle laser light-scattering detector (Wyatt, Santa Barbara, USA) and an Optilab dRI detector (Wyatt, Santa Barbara, USA). The column was pre-equilibrated in 20 mM HEPES pH 7.5 and 150 mM NaCl. Data analysis was carried out with Astra Version 8.2.2. For molecular mass calculation a dn/dc of 0.185 mL/g was assumed.

### TXTL assays

Plasmids encoding either the nuclease, a crRNA, deGFP or AcrVIB1 were used to assess the targeting activity of the nuclease and the inhibitory activity of AcrVIB1 in a cell-free transcription-translation (TXTL) assay. The nuclease was under the control of a T7 promoter; therefore a plasmid encoding the T7 RNA polymerase had to be added. The crRNA encoded either a targeting (T) spacer or non-targeting (NT) control. The assay is described in full previously.[25] In brief, we pre-expressed the AcrVIB1 plasmid in TXTL for 16 h with a final concentration of 4 nM, before adding the pre-expressed protein to fresh TXTL mix together with the plasmids encoding the Cas13b nuclease, a crRNA, T7RNAP or deGFP with a final concentration of 1 nM for the nuclease, the crRNA and deGFP and 0.2 nM T7RNAP. The samples were then incubated at 29°C for 16 h in a plate reader (BioTek Synergy H1), and fluorescence was measured every three minutes (excitation, emission: 485 nm, 528 nm). All TXTL reactions were prepared using the Echo525 Liquid Handling system to distribute the plasmids. The TXTL mix was distributed manually beforehand. Herein, a set of plasmids containing single amino-acid substitutions in either PbuCas13b or AcrVIB1 were tested for the impact on targeting and inhibitory activity, respectively. Mutations of PbuCas13b included K627A, N634A, and R662A. AcrVIB1 was mutated at three different sites, D37/38A, S56A, T70A. Furthermore, we tested four amino-acid substitutions in RanCas13b to test if they confer sensitivity to AcrVIB1 to the previously unaffected RanCas13b nuclease, K559N, Y609K, W627R and R630Q.

### *Quantification and statistical analysis*

In this study, unpaired, one-sided t tests, with the incorporation of Welch's correction, were employed to evaluate the statistical significance of observed differences between two independent groups. We employed these analyses for obtaining the statistical significance for crRNA degradation by RNase T1 and for binding measurements via MST.